Cell

Accumulation of the Inner Nuclear Envelope Protein Sun1 Is Pathogenic in Progeric and Dystrophic Laminopathies

Chia-Yen Chen,[1,8] Ya-Hui Chi,[5,8,*] Rafidah Abdul Mutalif,[6,8] Matthew F. Starost,[2] Timothy G. Myers,[3] Stasia A. Anderson,[4] Colin L. Stewart,[6,7] and Kuan-Teh Jeang[1,*]
[1]National Institute of Allergy and Infectious Diseases
[2]The Division of Veterinary Resources
[3]Genomic Technologies Section, Microarray Research Facility, National Institute of Allergy and Infectious Diseases
[4]National Heart, Lung, and Blood Institute Animal MRI Core
The National Institutes of Health, Bethesda, MD 20892, USA
[5]Institute of Cellular and System Medicine, National Health Research Institutes, Zhunan 35053, Taiwan, Republic of China
[6]Institute of Medical Biology, Singapore 138648, Singapore
[7]Department of Biological Science at the National University of Singapore, Singapore 117543, Singapore
[8]These authors contributed equally to this work
*Correspondence: ychi@nhri.org.tw (Y.-H.C.), kjeang@nih.gov (K.-T.J.)
DOI 10.1016/j.cell.2012.01.059

SUMMARY

Human *LMNA* gene mutations result in laminopathies that include Emery-Dreifuss muscular dystrophy (AD-EDMD) and Hutchinson-Gilford progeria, the premature aging syndrome (HGPS). The *Lmna* null (*Lmna*$^{-/-}$) and progeroid *Lmna*Δ9 mutant mice are models for AD-EDMD and HGPS, respectively. Both animals develop severe tissue pathologies with abbreviated life spans. Like HGPS cells, *Lmna*$^{-/-}$ and *Lmna*Δ9 fibroblasts have typically misshapen nuclei. Unexpectedly, *Lmna*$^{-/-}$ or *Lmna*Δ9 mice that are also deficient for the inner nuclear membrane protein Sun1 show markedly reduced tissue pathologies and enhanced longevity. Concordantly, reduction of SUN1 overaccumulation in *LMNA* mutant fibroblasts and in cells derived from HGPS patients corrected nuclear defects and cellular senescence. Collectively, these findings implicate Sun1 protein accumulation as a common pathogenic event in *Lmna*$^{-/-}$, *Lmna*Δ9, and HGPS disorders.

INTRODUCTION

The nuclear lamina that underlies the inner nuclear membrane (INM) is a meshwork of type-V intermediate filament proteins, consisting primarily of A- and B-type lamins (Güttinger et al., 2009). Mammalian somatic cells express four major types of lamins, including A and C encoded by *Lmna* (Burke and Stewart, 2006; Stuurman et al., 1998), and B1 and B2, each encoded by their own genes (*Lmnb1 and 2*) (Shimi et al., 2008; Stuurman et al., 1998). In addition to providing mechanical strength to the nucleus, recent discoveries in nuclear-lamina-associated human diseases have established intimate connections between the nuclear envelope/lamina and processes such as gene expression, DNA repair, cell cycle progression, and chromatin organization (Liu et al., 2005; Nagano and Arahata, 2000; Chi et al., 2009a; Capell and Collins, 2006; Worman and Courvalin, 2004).

Some 28 diseases/anomalies (the nuclear envelopathies) are linked to mutations in proteins of the nuclear envelope and lamina, and about half the diseases arise from mutations in the Lamin genes, predominately *LMNA*. These disease phenotypes range from cardiac and skeletal myopathies, lipodystrophies, and peripheral neuropathies to premature aging with early death (Burke and Stewart, 2002, 2006; Burke et al., 2001; Chi et al., 2009a; Worman and Courvalin, 2004). Two notable laminopathies are the autosomal-dominant form of Emery-Dreifuss muscular dystrophy (AD-EDMD), which results in muscle wasting and cardiomyopathy, and Hutchinson-Gilford progeria syndrome (HGPS), a rare genetic premature aging disease in which affected individuals expire with a mean life span of 13 years (Kudlow et al., 2007). AD-EDMD is caused by missense mutations and/or deletions throughout the *LMNA* gene that generally disrupt the integrity of the lamina, resulting in mechanical weakening of the nucleus and making it more vulnerable to mechanical stress. With HGPS, most cases arise from a single heterozygous mutation at codon 1824 of *LMNA*. This mutation produces an in-frame deletion of 50 amino acids and generates a truncated form of LAΔ50 lamin A, termed progerin, which remains farnesylated (De Sandre-Giovannoli et al., 2003; Eriksson et al., 2003; Goldman et al., 2004). HGPS individuals are overtly normal at birth, with the disease manifesting around 18 months (Merideth et al., 2008). The current view is that the permanently farnesylated progerin is affixed to the nuclear membrane and results in a toxic gain of function that elicits HGPS. How farnesylated progerin triggers HGPS is not understood.

Lmna$^{-/-}$ mice (Sullivan et al., 1999) were developed and found to model AD-EDMD. Subsequently, another mouse model was

created with homozygous $Lmna^{L530P/L530P}$ mutations in *Lmna* (later termed *Lmna*Δ9 mice; Hernandez et al., 2010; Mounkes et al., 2003) that expresses a deleted form of *Lmna* (deleted for exon 9 with the inframe removal of 40 amino acids of lamin A/C). There are distinct differences between $Lmna^{-/-}$, *Lmna*Δ9, and HGPS. The $Lmna^{-/-}$ mouse does not express a full-length lamin A protein, whereas the *Lmna*Δ9 mouse recapitulates many HGPS-associated pathologies including early death, skeletal anomalies, and vascular smooth muscle defects (Mounkes et al., 2003) and homozygously expresses a farnesylated lamin A-ΔExon9 mutant protein that, though similar, is not identical to the heterozygous expression of the LAΔ50 mutant protein in HGPS. Nonetheless, $Lmna^{-/-}$ and *Lmna*Δ9 mice and HGPS individuals share three significant features. All have *Lmna* mutations, significant dystrophic cellular, tissue and organ changes, and markedly abbreviated life spans.

Currently, although aberrant LAΔ50 progerin expression is implicated as causing HGPS, the full understanding of this and other causal events for lamin A-associated pathology is elusive. The lamins are proposed to interact with many INM proteins, including Emerin, lamina-associated polypeptides (LAPs) and MAN1, and the SUN domain proteins, SUN1 and SUN2 (Burke and Stewart, 2002; Mattioli et al., 2011; Crisp et al., 2006; Ostlund et al., 2009). A detailed biochemical understanding of these interactions is complicated by the relative insolubility of these proteins. The SUNs are components of the LINC (*l*inks the *n*ucleoskeleton and *c*ytoskeleton) complex that connect the nuclear lamina and envelope with the cytoskeleton (Crisp et al., 2006). The LINC complex is important in nuclear positioning and cellular migration in lower and higher eukaryotes (Malone et al., 1999). How the inner nuclear membrane SUN proteins function with lamins remains unclear, but currently there is no evidence that they are involved in laminopathies (Haque et al., 2010). Here we present evidence that $Lmna^{-/-}$, *Lmna*Δ9, and HGPS dysfunctions converge at a common pathogenic overaccumulation of the inner nuclear envelope Sun1 protein. Accordingly, loss of the *Sun1* gene in $Lmna^{-/-}$ and *Lmna*Δ9 mice extensively rescues cellular, tissue, organ, and life span abnormalities. Similarly, the knockdown of overaccumulated SUN1 protein in primary HGPS cells corrected their nuclear defects and cellular senescence. Our results reveal Sun1 overaccumulation as a potentially pivotal pathologic effector of some laminopathies.

RESULTS

Loss of Sun1 Ameliorates $Lmna^{-/-}$ and *Lmna*Δ9 Pathologies

To gain insight into the cooperativity, if any, between INM proteins and the underlying lamina in disease development, we bred $Sun1^{+/-}$ (Chi et al., 2009b) and $Lmna^{+/-}$ (Sullivan et al., 1999) mice to produce $Lmna^{-/-}Sun1^{-/-}$ offspring. A priori, it was anticipated that inactivating both *Lmna* and *Sun1* in $Lmna^{-/-}Sun1^{-/-}$ mice would lead to a more severe pathological phenotype than that seen for $Lmna^{-/-}$ animals. Surprisingly, we observed the opposite. In the $Lmna^{-/-}$ context, the removal of *Sun1*, rather than exacerbating pathology, unexpectedly ameliorated deficits in body weight (Figure 1A; $p < 0.0001$) and longevity (Figure 1B; $p < 0.01$). This rescue of $Lmna^{-/-}$ mice by loss of Sun1 was verified in a second laminopathy model, the *Lmna*Δ9 mutant mouse (Mounkes et al., 2003; Hernandez et al., 2010). The body weight and longevity deficits in *Lmna*Δ9 mice were also rescued in the *Lmna*Δ9$Sun1^{-/-}$ counterparts (Figures 1C and 1D). Remarkably, whereas all *Lmna*Δ9 mice expired by 30 days after birth, their *Lmna*Δ9$Sun1^{-/-}$ littermates thrived past this date, and most achieved life spans more than twice this duration (Figure 1D). At the cellular level, the severely reduced proliferation of $Lmna^{-/-}$ and *Lmna*Δ9 fibroblasts was also substantially corrected in $Lmna^{-/-}Sun1^{-/-}$ and *Lmna*Δ9$Sun1^{-/-}$ cells (Figures 1E and 1F).

Tissue Pathologies Are Improved in $Sun1^{-/-}Lmna^{-/-}$ Mice

$Lmna^{-/-}$ and $Lmna^{-/-}Sun1^{-/-}$ animals grow to a greater size and live longer than their corresponding *Lmna*Δ9 and *Lmna*Δ9$Sun1^{-/-}$ counterparts (Figures 1A–1D). Cultured $Lmna^{-/-}$ and $Lmna^{-/-}Sun1^{-/-}$ cells proliferated well, whereas *Lmna*Δ9 and *Lmna*Δ9$Sun1^{-/-}$ cells are challenging, requiring extracellular matrices or hypoxic conditions for propagation (Hernandez et al., 2010). For detailed characterizations, we chose to study the $Lmna^{-/-}$ and $Lmna^{-/-}Sun1^{-/-}$ animals and their cells.

We compared tissue changes in $Lmna^{-/-}$ to $Lmna^{-/-}Sun1^{-/-}$ mice. The spine of $Lmna^{-/-}$ mice by microcomputerized tomography was grossly lordokyphotic; this defect was absent in wild-type (WT) and $Sun1^{-/-}$ mice and was corrected in $Lmna^{-/-}Sun1^{-/-}$ animals (Figure 2A). The femoral bone of 40-day-old $Lmna^{-/-}$ mice showed trabecular and bone densities that were notably sparser and thinner than in $Sun1^{-/-}$ or WT mice; in $Lmna^{-/-}Sun1^{-/-}$ animals, the deficits were markedly improved (Figure 2B). In other tissues, such as cardiac and skeletal muscle, pathologies, previously described in the $Lmna^{-/-}$ mice, were corrected and improved in the $Lmna^{-/-}Sun1^{-/-}$ mice (Figure S1 available online).

Sun1 Accumulates at the Nuclear Envelope and the Golgi of $Lmna^{-/-}$ MEFs

To seek a molecular explanation for loss-of-lamin A changes and their correction by Sun1 depletion, we investigated Sun1 expression in lamin A WT and $Lmna^{-/-}$ mouse embryonic fibroblasts (MEFs). Sun1 and lamin A colocalize at the Nuclear Envelope (NE) in WT MEFs (Figure 3A, left panels). In contrast, in $Lmna^{-/-}$ MEFs, Sun1 is found in the NE and at increased levels in the Golgi (Figure 3A, middle panels; Figure S2A) based on costaining with Golgi marker GM130 (Figure S2A, right), but not with ER marker calnexin (Figure S2A, left). NE localization and Golgi overaccumulation of Sun1 were also seen in *Lmna*Δ9 mouse fibroblasts (Figure S2A, right). That Sun1 localizes with Golgi constituents in $Lmna^{-/-}$ cells was supported by biochemical fractionation of mouse tissues that detected Sun1 and GM130 in the same sucrose density fractions (Figure S2B). When $Lmna^{-/-}$ cells were examined for the relative distribution of Sun1 in the NE versus the Golgi, the amount in the latter increased proportionally with its level in the former (Figure S2C), suggesting that increased levels of Sun1 protein, in an $Lmna^{-/-}$ context, first occupy and saturate NE sites before "spilling" into the Golgi compartment. The average Sun1 expression level in individual

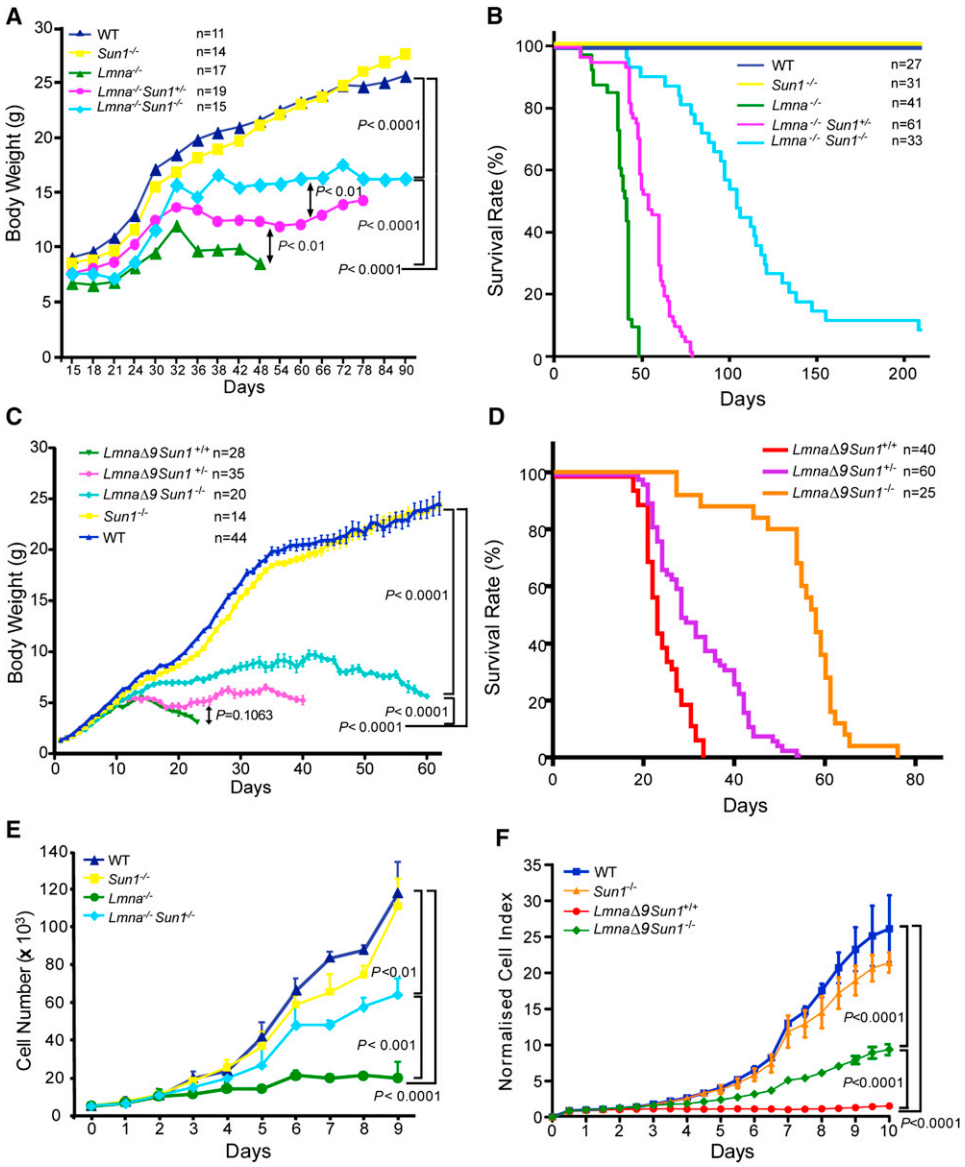

Figure 1. Defects in Body Weight and Longevity in *Lmna*$^{-/-}$ and *Lmna*Δ9 Mice Are Ameliorated in Homozygous Sun1 Knockout *Lmna*$^{-/-}$*Sun1*$^{-/-}$ and *Lmna*Δ9*Sun1*$^{-/-}$ Animals

(A) Body weights are averages from mice with the indicated genotypes. The number (n) of animals used is indicated.

(B) Kaplan-Meier graph showing increased life span of *Lmna*$^{-/-}$*Sun1*$^{-/-}$ compared to *Lmna*$^{-/-}$ mice. Median survival of wild-type or *Sun1*$^{-/-}$ is > 210 days in a 7 month follow up; *Lmna*$^{-/-}$ mice have median survival of 41 days; *Lmna*$^{-/-}$*Sun1*$^{+/-}$ mice have a median survival of 54 days; *Lmna*$^{-/-}$*Sun1*$^{-/-}$ mice have a median survival of 104 days ($p < 0.01$ comparing *Lmna*$^{-/-}$ and *Lmna*$^{-/-}$*Sun1*$^{-/-}$.)

(C) Body weights of *Lmna*Δ9 mice that are wild-type, heterozygous, or homozygous for *Sun1* deficiency. Wild-type and *Sun1*$^{-/-}$ cohorts are graphed for comparison. Values are averages ±SEM from animals in each cohort. Number (n) of animals is indicated. ($p < 0.0001$ comparing *Lmna*Δ9*Sun1*$^{+/+}$ and *Lmna*Δ9*Sun1*$^{-/-}$.)

(D) Kaplan-Meier graph showing increased life span of *Lmna*Δ9*Sun1*$^{-/-}$ compared to *Lmna*Δ9*Sun1*$^{+/+}$ mice. *Lmna*Δ9*Sun1*$^{+/-}$ mice are also graphed. ($p < 0.0001$ comparing *Lmna*Δ9*Sun1*$^{+/+}$ and *Lmna*Δ9*Sun1*$^{-/-}$.)

(E) Cell proliferation of the indicated MEFs. Curves are averages ±SD, representative of > 3 independent isolates from embryos of the indicated genotypes.

(F) Proliferation curves of MAFs (mouse adult fibroblasts) from WT, *Sun1*$^{-/-}$, *Lmna*Δ9*Sun1*$^{+/+}$ and *Lmna*Δ9*Sun1*$^{-/-}$ mice. MAFs were seeded at a density of 1000 cells per well. Growth was measured, and normalized cell indexes (averages+/−SD) are presented.

Lmna$^{-/-}$ MEFs was significantly higher than that in WT MEFs (Figure 3B; *Lmna*$^{-/-}$ $n = 36$, WT n = 29, $p < 0.0001$), and the highest expressing former cells had approximately 8-fold greater levels of Sun1 than the lowest expressing latter counterparts; in contrast, in *Lmna*$^{-/-}$ cells, other NE proteins such as Sun2 and Nup153 were unchanged in distribution or amounts,

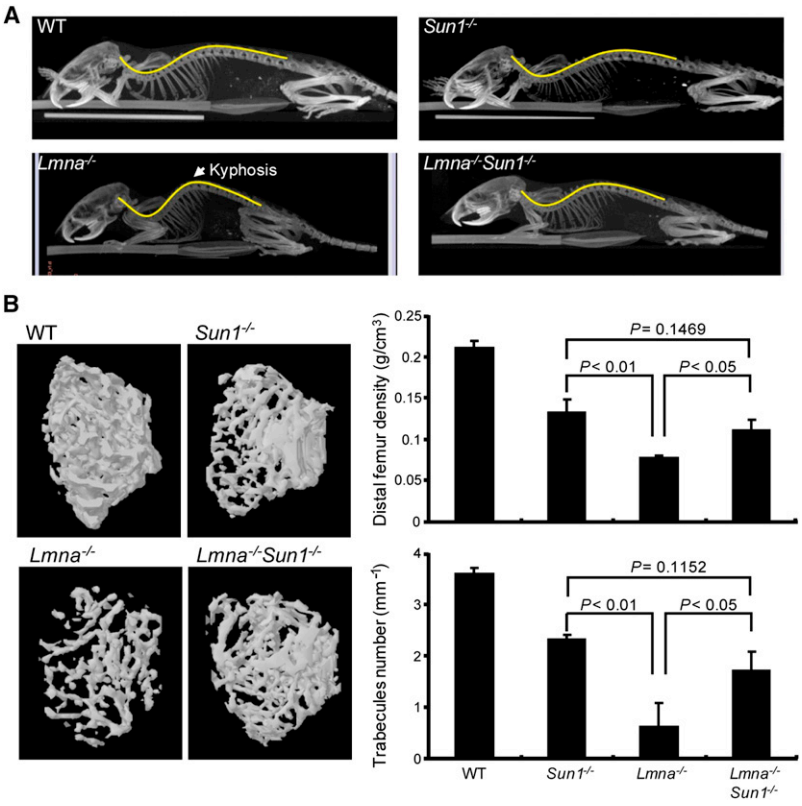

Figure 2. Correction of the *Lmna*$^{-/-}$ Skeletal Defects in the *Lmna*$^{-/-}$*Sun1*$^{-/-}$ Double-Knockout Mouse

(A) Micro-CT scans of the indicated mice. *Lmna*$^{-/-}$ mice display a lordokyphosis (curvature of the spine) phenotype corrected in *Lmna*$^{-/-}$*Sun1*$^{-/-}$ mice.

(B) Three-dimensional micro-CT images of the femoral trabeculae from 40-day-old mice (left). Thinner trabecular formation was observed in the *Lmna*$^{-/-}$ mouse compared to the other genotypes. Right panels quantify bone density+/−SD (upper) and the number of trabeculaes/mm+/−SD (lower). P values are shown. See also Figure S1.

whereas Emerin and Nesprin1 were not significantly increased but showed modest increases in ER relocalization (Figures S2D and S2E). The increase in Sun1 protein (Figure S2E) was not due to elevated Sun1 mRNA levels (compare WT and *Lmna*$^{-/-}$; Figure S2F). This result, together with heightened Sun1 accumulation (Figure S3A) when WT and *Lmna*$^{-/-}$ MEFs were treated with proteasome inhibitor lactacystin and the prolonged half-life of Sun1 protein in *Lmna*$^{-/-}$ versus WT MEFs (Figure S3B), suggests that Sun1 overaccumulation in *Lmna*$^{-/-}$ cells is due to reduced protein turnover.

Sun1 Overaccumulation Increases Nuclear Defects

WT MEFs have circular or slightly ovoid nuclei, whereas *Lmna*$^{-/-}$ nuclei are irregularly shaped with frequent herniations and blebs (Figure 3C) (Sullivan et al., 1999). Intriguingly, *Lmna*$^{-/-}$ nuclear abnormalities are significantly reduced ($p < 0.0001$) in *Lmna*$^{-/-}$*Sun1*$^{-/-}$ cells (Figures 3C and 3D), suggesting that the nuclear irregularities are not explained simply by loss of lamin A, which is equally absent in *Lmna*$^{-/-}$ and *Lmna*$^{-/-}$*Sun1*$^{-/-}$ cells. On the other hand, because both *Lmna*$^{-/-}$ and *Lmna*Δ9 cells show Sun1 accumulation in the Golgi (Figure 3A and Figure S2A), this event could possibly account for the observed pathologies. This view, if correct, provides a parsimonious explanation for why *Lmna*$^{-/-}$ and *Lmna*Δ9 diseases in mice are alleviated when *Sun1* levels are reduced (Figure 1).

The above reasoning predicts that deliberate Sun1 overexpression in an *Lmna*$^{-/-}$ context should exacerbate nuclear aberrancies. To test this, we transfected increasing amounts of a mouse Sun1 (mSun1) expression vector into either *Lmna*$^{-/-}$*Sun1*$^{-/-}$ or WT MEFs. The overexpression of Sun1 progressively increased the prevalence of nuclear herniations in *Lmna*$^{-/-}$*Sun1*$^{-/-}$ MEFs without significantly affecting WT MEFs (Figure 3E). The transfections also elicited dose-dependent increases in the apoptosis of *Lmna*$^{-/-}$*Sun1*$^{-/-}$ cells (Figure 3F).

Golgi Targeting of Sun1 Elicits Nuclear Herniations

A remarkable feature of Sun1 expression in *Lmna*$^{-/-}$ MEFs is its misaccumulation in the extranuclear Golgi apparatus (Figure 3A and Figure S2A). Protein misaccumulation in human organelle storage disorders has been described for lysosomal storage diseases such as Fabry, Tay-Sachs, Gaucher, Niemann-Pick, Pompe, and Krabbe (Metz et al., 2011) and for endoplasmic reticulum storage diseases such as cystic fibrosis, α1-antitrypsin deficiency, hereditary hypoparathyroidism, and procollagen type I, II, and IV deficiency (Rutishauser and Spiess, 2002); however, to date, there are no good examples of Golgi storage diseases. To test whether the deliberate Golgi misaccumulation of Sun1 is significantly pathogenic, we constructed an HA-tagged Tgn38-fused Golgi-targeting mSun1 expression vector (Tgn38 is an integral Golgi protein; see Szentpetery et al. [2010]). Sun1 protein, when overexpressed in WT MEFs, localized to the nuclear envelope and elicited barely discernable mild nuclear blebbings (Figure 4A), whereas transfected Tgn38-Golgi-targeted mSun1 dramatically increased Golgi accumulation and nuclear herniations with obvious cytoplasmic accumulation of lamin B1 (Figure 4B) in 83% of Tgn38-Golgi-mSun1 expressing cells (Figure 4C). Recently, it was reported that the Sun1-related Sun2 protein has a Golgi retrieval signal, ensuring its transport from the Golgi back to the ER (Turgay et al., 2010). Although not yet determined, Sun1 may differ in the Golgi retrieval signal, which could explain why a SUN1 mutant (human SUN1 [aa] 103–785) (Figure S4; Haque et al., 2010; Chi et al., 2007) and a wild-type Sun1 protein that is expressed in the absence of cell endogenous lamin A (i.e., *Lmna*$^{-/-}$ cells; Figures 3A and S2A) are both found in the Golgi. We also checked whether the Golgi-localizing SUN1 (103–785) mutant

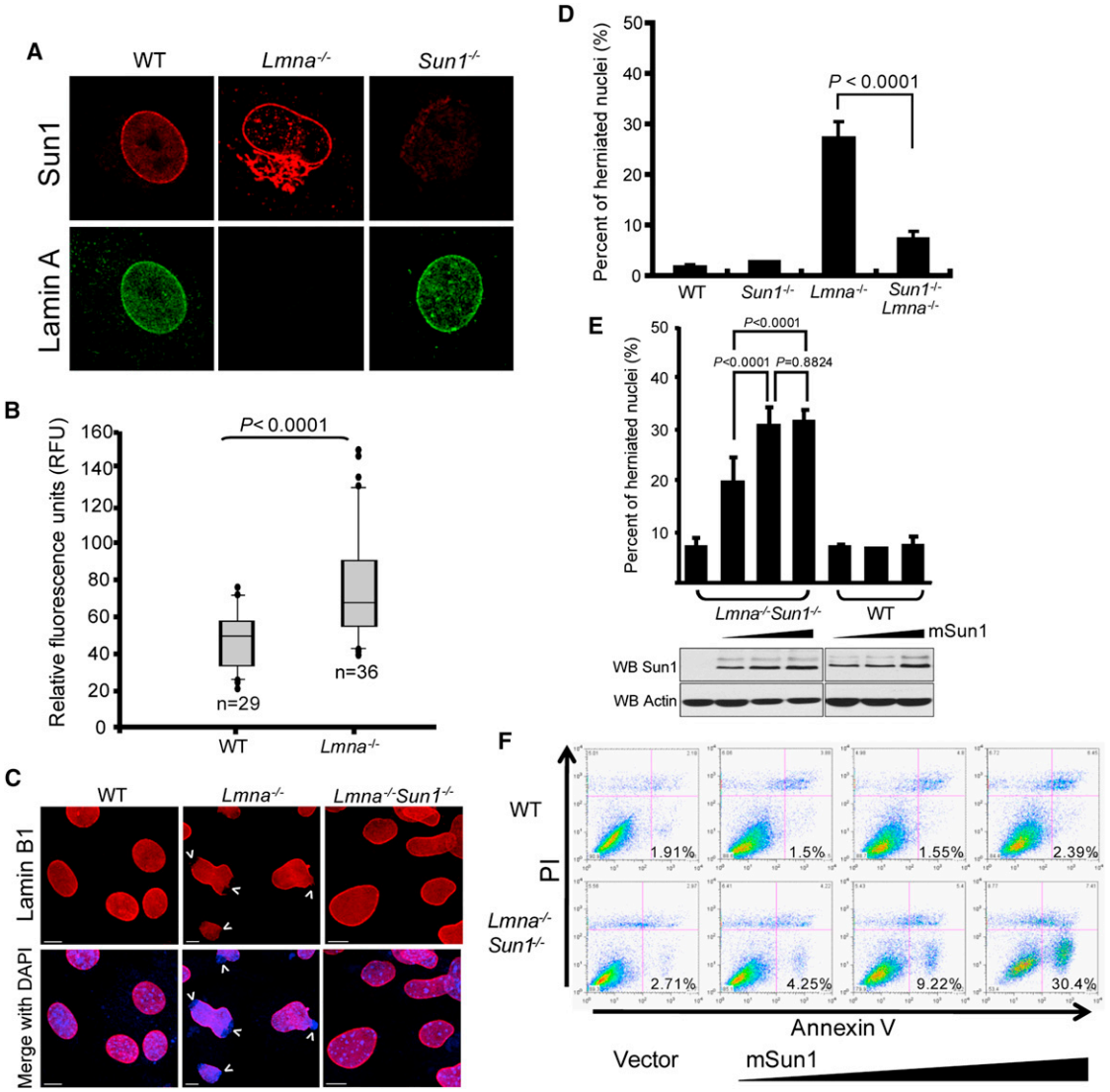

Figure 3. Extranuclear Sun1 Is Accumulated in the Golgi of *Lmna*$^{-/-}$ MEFs

(A) Cells were immunostained with lamin A (green) and Sun1 (red) antibodies. Extranuclear Golgi localization of Sun1 is seen in *Lmna*$^{-/-}$ MEFs. See also Figure S2.

(B) Quantification of Sun1 in MEFs. Mean ± SD reflects collective results from two separate experiments with n = 29 (WT) and n = 36 (*Lmna*$^{-/-}$) MEFs. Difference between WT and *Lmna*$^{-/-}$ is statistically significant ($p < 0.0001$). See also Figure S3.

(C) WT, *Lmna*$^{-/-}$, and *Lmna*$^{-/-}$*Sun1*$^{-/-}$ MEFs were stained with anti-Lamin B1 (red) and DAPI (blue). Lamin B1 nuclear envelope staining is intact in WT and *Lmna*$^{-/-}$*Sun1*$^{-/-}$ MEFs, with the staining being irregular with herniations in *Lmna*$^{-/-}$ nuclei. Arrows point to disruptions in nuclear envelope. Scale bars, 10 μm.

(D) Quantification of prevalence of cells with nuclear envelope disruptions. Values are averages +/−SD from three independently isolated MEFs of the indicated genotype (each counted for 300 nuclei). Prevalence of nuclear disruptions between *Lmna*$^{-/-}$ and *Lmna*$^{-/-}$*Sun1*$^{-/-}$ MEFs is significantly different ($p < 0.0001$).

(E) Sun1 overexpression in the absence of lamin A exacerbates nuclear herniations (upper). WT and *Lmna*$^{-/-}$*Sun1*$^{-/-}$ MEFs were transfected with increasing mouse Sun1 (mSun1) expression vector. Nuclei were stained 48 hr later. Values are averages +/−SD from three experiments (each sample was counted for 300 nuclei per experiment). (Lower) Transfected cells were western blotted for Sun1 expression and actin (as loading control).

(F) WT (top) or *Lmna*$^{-/-}$*Sun1*$^{-/-}$ (bottom) MEFs were transfected with vector-alone (left) or increasing amounts of mSun1 (right three panels) and analyzed 48 hr later by FACS for propidium iodide (PI; y axis) and annexin V (x axis). Percentage of apoptotic cells (in the lower right quadrant) is indicated.

elicits nuclear aberrations. Indeed, overexpression of the SUN1 (103-785) mutant increased nuclear envelope rupture and cytoplasmic redistribution of lamin B1 (Figure S4).

The above results suggest that reducing Sun1 accumulation in the Golgi might moderate *Lmna*$^{-/-}$ nuclear irregularities. Brefeldin A (BFA) is an antibiotic that reversibly interferes with the anterograde transport of macromolecules from the endoplasmic reticulum (ER) to the Golgi (Marie et al., 2008). We asked whether BFA treatment of *Lmna*$^{-/-}$ cells would reduce Sun1 in the Golgi. Confocal imaging of *Lmna*$^{-/-}$ MEFs treated with

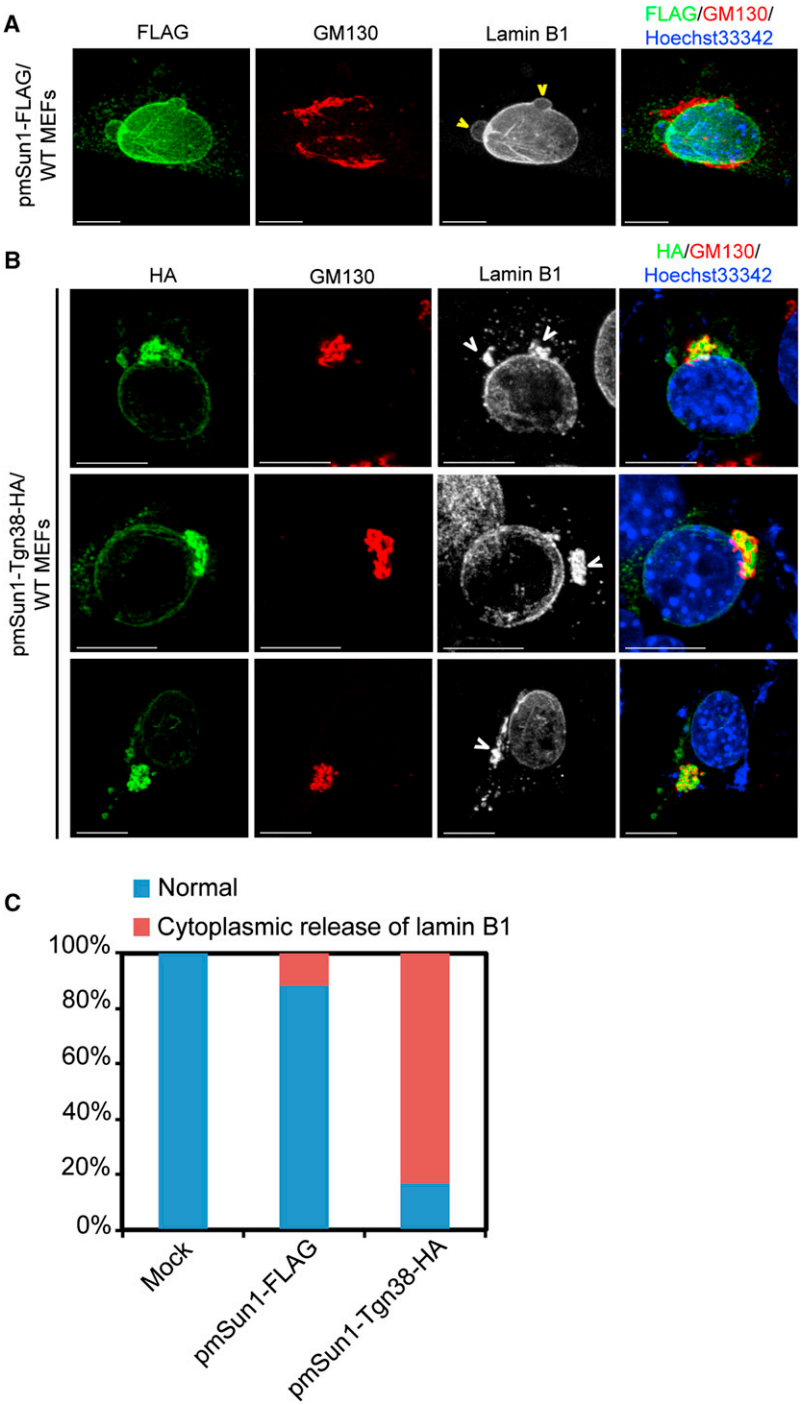

Figure 4. Overexpression of Golgi-Targeted Sun1 Increased Nuclear Aberrations and Cell Death

(A) WT MEFs were transfected with FLAG-tagged mouse Sun1 vector and stained with mouse anti-FLAG (green), rabbit anti-GM130 (red), and goat anti-lamin B1 (grayscale). A representative image of modest nuclear blebs and ruffles seen in some transfected cells is shown. Scale bars, 10 μm.

(B) A Golgi-targeted mouse Sun1 (fused with Tgn38, HA-tagged) expression plasmid was transfected into WT MEFs. Thirty hours later, cells were stained with mouse anti-HA (green), rabbit anti-GM130 (red), and goat anti-lamin B1 (grayscale). Aberrancies were visualized by cytoplasmic lamin B1 staining (see arrowheads) of pmSun1-Tgn38-HA transfected cells. Scale bars, 10 μm.

(C) Quantification of the cytoplasmic release of lamin B1 in MEFs transfected (for 30 hr) with either mSun1 (mSun1-FLAG) or the Golgi-targeted mSun1 (pmSun1-Tgn38-HA). One hundred cells were counted in each case. See also Figure S4.

BFA at 10 μg/ml for 24 hr showed a reduction in most, albeit not all, Golgi-trafficked Sun1 and GM130 proteins (Figure 5A, left) with statistically significant ($p < 0.001$; $p < 0.01$) reduction in nuclear aberrations in cells passaged four (P4) to eight (P8) times in culture (Figure 5A, right graph). We also treated *Lmna*$^{-/-}$ MEFs with nocodazole to block microtubule organization (Figure 5B) or latrunculin B to interrupt actin assembly (Figure 5C). Nocodazole disrupts the Golgi apparatus (Thyberg and Moskalewski, 1999), and its treatment of *Lmna*$^{-/-}$ MEFs led to a punctated redistribution of otherwise Golgi-associated Sun1 and GM130 (Figure 5B). This treatment also led to a moderate, but statistically significant, reduction of nuclear aberrations (Figure 5B, right graph). In contrast, latrunculin B did not affect Sun1 distribution in the Golgi or ameliorate nuclear defects (Figure 5C). Collectively, the findings demonstrate that endogenous (Figure 5) or exogenous (Figures 4 and S4) Sun1 misaccumulation in the Golgi elicits substantial cellular pathologies, and that reducing Sun1 Golgi accumulation restores cellular normalcy.

SUN1 Overaccumulation in HGPS Cells Correlates with Dysfunction

We next investigated SUN1 expression in HGPS cells, querying whether (and how) this protein might contribute to pathology. We immunostained SUN1 expression in human skin fibroblasts from seven independent HGPS (*LMNA* c.1824C>T [G608G]) (Figure S5A and Table S1) and four normal individuals and verified LAΔ50 progerin expression (Goldman et al., 2004) in HGPS, but not in normal, cells (Figure S5B). By immunofluorescence, brighter SUN1 staining was observed in HGPS cells compared to control cells (representative examples are in Figure 6A and Figure S5A; normal versus HGPS), which is consistent with increased SUN1 expression by western blotting (Figure S5B) and with an earlier report of SUN1 accumulation in HGPS cells (Haque et al., 2010). Of note, our stainings showed that not every HGPS cell had elevated SUN1, but that cells that stained brightest for SUN1 were also ones that had larger nuclei and more severe nuclear morphological distortions (compare dim-SUN1 HGPS cells, white arrowheads to

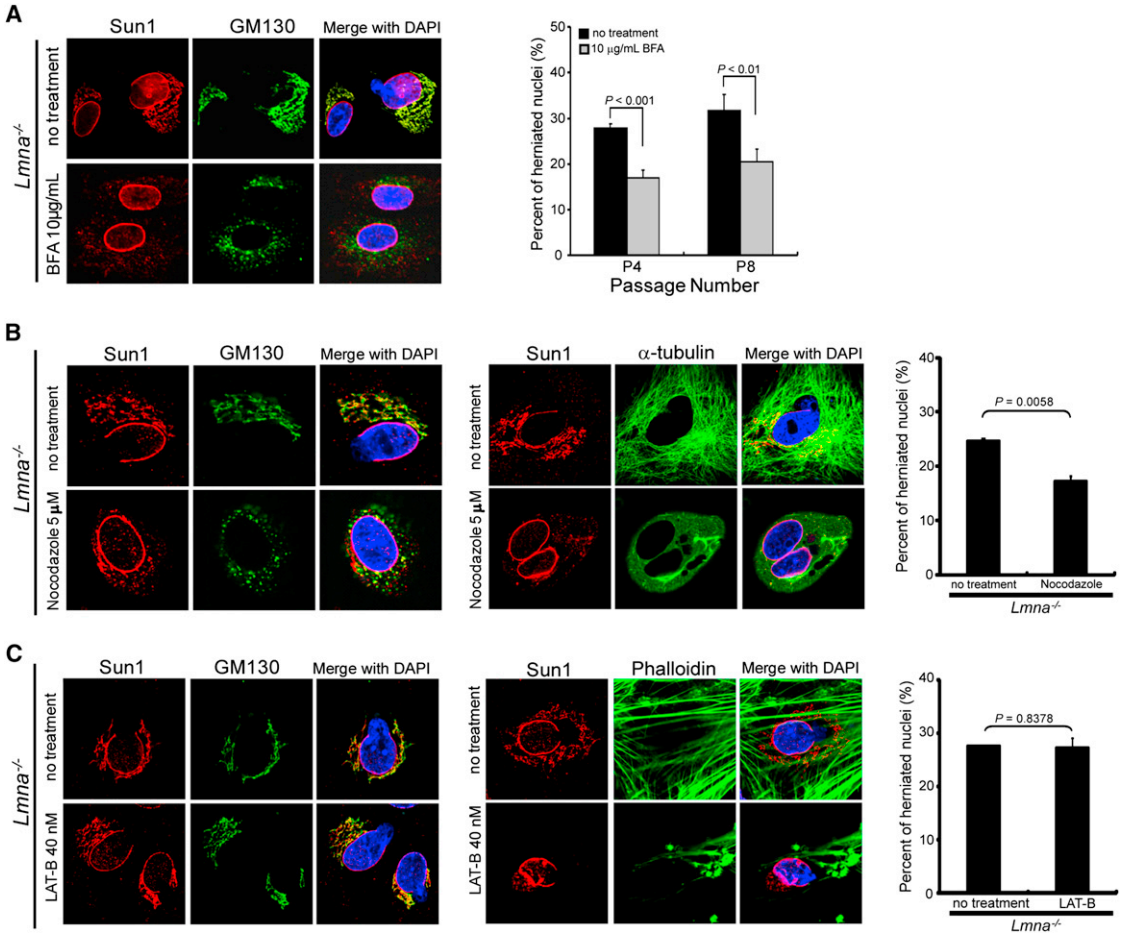

Figure 5. Brefeldin A and Nocodazole, but Not Latrunculin, Treatment Reduced Nuclear Irregularities in *Lmna*$^{-/-}$ MEFs

(A) (Left) Staining of Sun1 (red) and GM130 (green) in *Lmna*$^{-/-}$ MEFs treated for 24 hr with brefeldin A (BFA; 10 μg/ml); note the reduction of Sun1 and GM130 from the Golgi. (Right) Quantification of BFA treatment on the nuclear morphology of *Lmna*$^{-/-}$ MEFs. Untreated and treated cells were stained with mouse Sun1-specific antibody or DAPI in cells passaged 4 (P4), and 8 (P8) times, respectively. The nuclear morphology was evaluated by observers blinded for genotype and by computerized image analyses. Nuclear irregularities are also seen in HGPS cells (see list in Table S1).

(B) (Left) Subcellular localization of Sun1 in *Lmna*$^{-/-}$ MEFs untreated or treated with 5 μM nocodazole for 4 hr. The Golgi complex was stained with mouse antibody against GM130 (green) and rabbit antibody against mouse Sun1 (red). (Middle) Cells untreated and treated with nocodazole and stained for α-tubulin are shown. (Right) Quantification of nocodazole treatment on the nuclear morphology of *Lmna*$^{-/-}$ MEFs. Difference between untreated and treated cells is p = 0.0058.

(C) (Left) *Lmna*$^{-/-}$ MEFs were untreated or treated with 40 nM of latrunculin (LAT-B) for 12 hr. Cells were fixed and stained for Sun1 and GM130. (Middle) Cells untreated and treated with latrunculin and visualized with fluorescent phalloidin for actin are shown. (Right) Quantification of LAT-B treatment on the nuclear morphology of *Lmna*$^{-/-}$ MEFs. Difference between untreated and treated cells was statistically insignificant (p = 0.8376). All values are mean +/−SD.

bright-SUN1 HGPS cells, yellow arrowheads; Figure 6A). *SUN1* mRNA levels did not differ significantly in HGPS versus normal cells (Figure S5C), supporting the interpretation that reduced protein turnover (Figure S3B), not increased transcription, underlies SUN1 accumulation.

To address whether elevated SUN1 levels in HGPS result in pathologies, we asked whether knocking down SUN1 alleviates nuclear defects. SUN1-specific or control siRNAs were transfected into HGPS or normal skin fibroblasts, and nuclear appearance was monitored (Figure S5D). The nuclear morphologies were unchanged in cells treated with control siRNA (Figures 6B and S5E), but SUN1-specific siRNA reduced the prevalence of bright-SUN1 HGPS cells (compare AG11498 upper to lower row, Figures 6B and 6C) and lowered the number of cells with aberrant nuclei (Figures 6B, 6D, and S5E; Table S1). The contribution of SUN1 to nuclear morphology was assessed conversely by deliberately overexpressing exogenous SUN1. Ectopic SUN1 overexpression in HGPS and normal fibroblasts significantly increased aberrant nuclei (Figure 6E).

SUN1 Expression Correlates with HGPS Heterochromatin Profile and Cellular Senescence

Chromatin disorganization and massive heterochromatin loss are correlated with nuclear shape alterations in HGPS cells (Shumaker et al., 2006; Goldman et al., 2004). Assays for HGPS heterochromatin loss have included markers such as the lamin

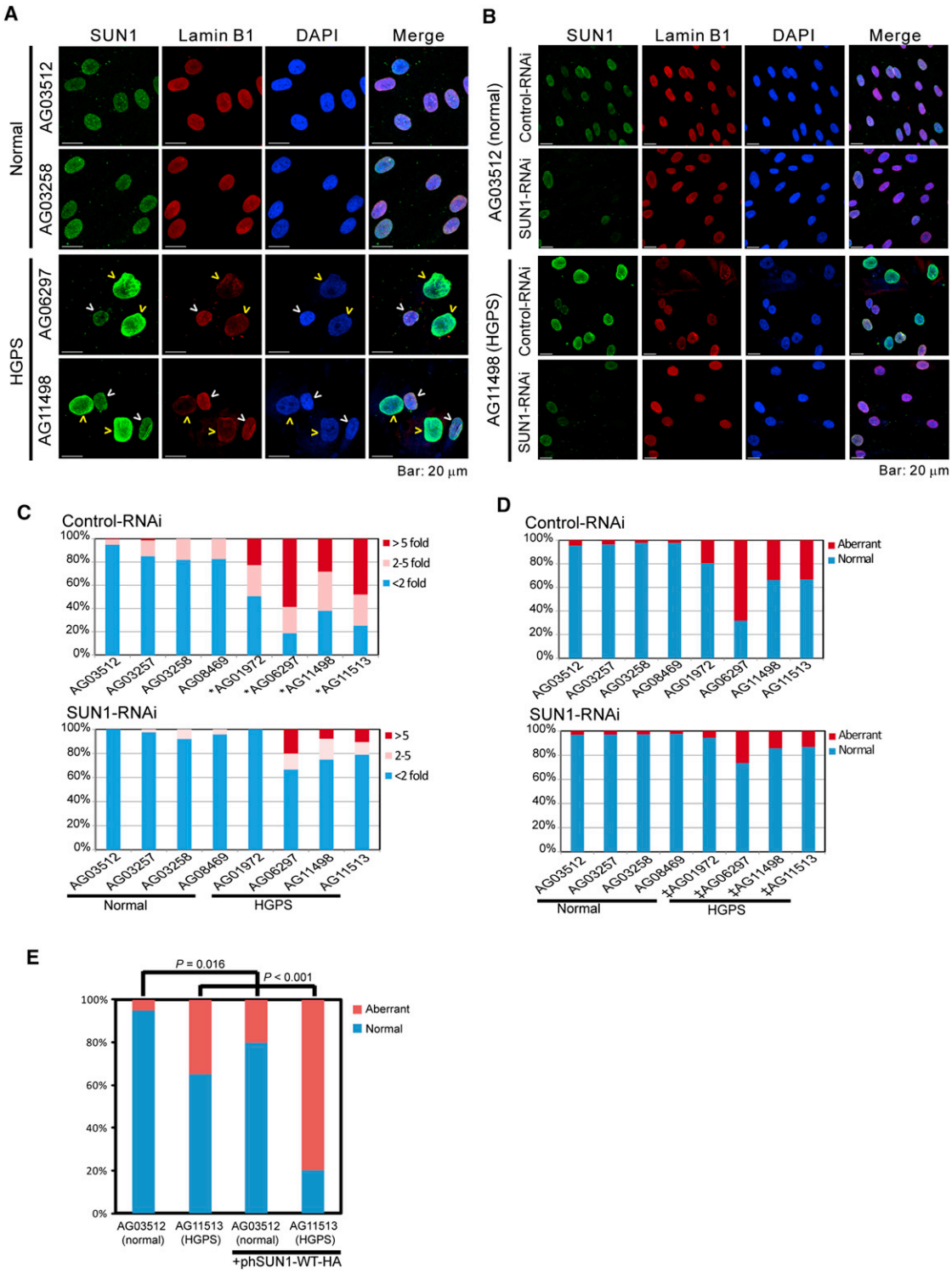

Figure 6. Nuclear Irregularities in HGPS Fibroblasts Correlate with SUN1 Expression

(A) SUN1 and lamin B1 in normal (AG03512 and AG03258) and HGPS (AG06297 and AG11498) skin fibroblasts are stained with anti-human SUN1 (green) and anti-lamin B1 (red). DAPI is in blue. Yellow arrowheads point to cells expressing high SUN1, white arrowheads to cells with low SUN1.

(B) Nuclear morphologies and SUN1 staining of control (AG03512) and HGPS (AG11498) skin fibroblasts transfected with control or SUN1 siRNA for 72 hr.

(C) Quantification of SUN1 immunofluorescent intensities in cells treated with control or SUN1 siRNA. One hundred twenty to two hundred cells from each of the indicated samples were visualized and quantified for staining intensities. The intensities were normalized to the SUN1 intensity in AG03512 cells. Cells with SUN1

A-associated NURD (*nu*cleosome *r*emodeling and *d*eacetylase) component RBBP4 (Pegoraro et al., 2009) and the pan heterochromatin marker histone H3K9me3 (Shumaker et al., 2006; Scaffidi and Misteli, 2005). To corroborate the nuclear morphology findings (Figure 6), we investigated how SUN1 expression correlates with previously described HGPS heterochromatin changes. When HGPS or normal-skin fibroblasts were stained for RBBP4 (Figure 7A, left) or H3K9me3 (Figure 7A, right), an inverse correlation was observed between the expression of SUN1 and RBBP4 (Figure 7B, left) or H3K9me3 (Figure 7B, right). In agreement with the results in Figure 6A, only a subset of HGPS cells was bright SUN1 (yellow arrows = bright-SUN1, white arrows = dim-SUN1; Figure 7A); interestingly, the bright-SUN1 cells were also those with the larger, more distorted nuclei as well as sparse staining for RBBP4 (Figures 7A and 7B, left) or H3K9me3 (Figures 7A and 7B, right). Separately, we found that RBBP4 expression was substantially reduced in ~70% of *Lmna*$^{-/-}$ MEFs (Figure S6A) and in *Lmna*$^{-/-}$ mouse liver tissue (Figure S6B), further supporting an inverse relationship between Sun1 and NURD activity.

We next asked whether knockdown of SUN1 would reverse HGPS-associated heterochromatin changes. We compared control-RNAi and SUN1-RNAi transfected HGPS cells and found that the latter did recover RBBP4 expression relative to the former (Figure 7C). Because heterochromatin dysregulation is correlated with cellular senescence (Di Micco et al., 2011) and because HGPS cells senesce prematurely (DeBusk, 1972; Eriksson et al., 2003), we queried how SUN1 affects HGPS senescence by knocking down SUN1 for 96 hr and examining acidic senescence-associated β-galactosidase (SA-β-Gal) in control and HGPS cells (Figure 7D). In normal cells, the extent of senescence was similar (~9%) between control-siRNA and SUN1-siRNA samples (Figure 7D); however, in HGPS cells, the observed high level of ambient senescence (~22%), as measured by β-galactosidase, was dramatically decreased (to ~6%) after SUN1 knockdown. Moreover, HGPS fibroblasts, when treated with SUN1-RNAi, gained a proliferative advantage over control-RNAi treated cells (Figure 7E). These data collectively support the interpretation that increasing SUN1 accumulation is associated with HGPS pathology and removing overexpressed SUN1 and restores normal cellular physiology.

DISCUSSION

Here, we show that aberrant Sun1 expression is a critical pathogenic event common to *Lmna*$^{-/-}$, *Lmna*Δ9, and HGPS disorders. As noted here and elsewhere, *Lmna*$^{-/-}$ mice (Sullivan et al., 1999), *Lmna*Δ9 mice (Hernandez et al., 2010; Mounkes et al., 2003), and HGPS individuals (Merideth et al., 2008) share a constellation of disorders that include nuclear aberrations, dystrophic organ and tissue abnormalities, and abbreviated life spans. A current view is that progerin is causal of the LAΔ50 HGPS disease (Burtner and Kennedy, 2010; Liu et al., 2005; Scaffidi and Misteli, 2005; Goldman et al., 2004). How progerin mechanistically signals cellular and tissue damage remains elusive. That said, the existence of the dystrophic and cardiomyopathic pathologies in *Lmna*$^{-/-}$ mice and multiple examples of *Lmna* mutations (Novelli et al., 2002; Plasilova et al., 2004; Sullivan et al., 1999) that do not synthesize progerin but do produce degenerative-dystrophic diseases such as Emery-Dreifuss muscular dystrophy (Bonne et al., 1999), Charcot-Marie-Tooth (De Sandre-Giovannoli et al., 2002; Chaouch et al., 2003), Mandibuloacral dysplasia (Novelli et al., 2002), Dunnigan-type familial partial lipdystrophy (Cao and Hegele, 2000), atypical Werner's syndrome (Chen et al., 2003), and limb girdle muscular dystrophy (Muchir et al., 2000; Kitaguchi et al., 2001), require an understanding of progerin-independent and dependent factors/cofactors underlying the pathologies.

The Sun1 protein connects the nucleoplasm with the cytoskeleton (Crisp et al., 2006) and has roles in nuclear anchorage, nuclear migration, and cell polarity. Deficits in Sun1 correlate with developmental retardation in neurogenesis, gametogenesis, myogenesis, and retinogenesis (Ding et al., 2007; Lei et al., 2009; Zhang et al., 2009; Yu et al., 2011; Chi et al., 2009b). To date, how an inner nuclear envelope protein like Sun1 fits into the pathogenesis of laminopathies is unknown (Stewart et al., 2007).

The major unexpected finding here is that whereas *Lmna*$^{-/-}$ mice and *Lmna*Δ9 mice thrive poorly and die prematurely, the removal of *Sun1*, creating *Lmna*$^{-/-}$*Sun1*$^{-/-}$ and *Lmna*Δ9*Sun1*$^{-/-}$ mice, rescued pathologies and dramatically improved longevity (Figures 1 and 2). To better understand these results, we observed that at the cellular level, *Lmna*$^{-/-}$ and *Lmna*Δ9 fibroblasts have uniformly increased Sun1 expression with significant protein misaccumulation in the Golgi (Figure 3A and Figure S2). Furthermore, approximately one in three LAΔ50 HGPS fibroblasts (Figures 6, 7, and S5; Table S1) was elevated for SUN1 expression with the bright (high)-SUN1, but not the dim (low)-SUN1, cells, exhibiting abnormal nuclear size and shape, heterochromatin RBBP4 and H3K9me3 markers, and cellular senescence (Figures 6 and 7). Even though one cannot do a *SUN1* knockout experiment in LAΔ50 HGPS individuals, the knockdown of SUN1 in LAΔ50 HGPS cells considerably improved nuclear size and/or shape defects, heterochromatin loss, and cellular senescence (Figures 6 and 7). Thus, although the approaches (knockout and knockdown) and disease models (*Lmna*$^{-/-}$, *Lmna*Δ9, and LAΔ50 HGPS) are not identical, a parsimonious interpretation consistent with the collective results is that Sun1 overaccumulation represents a common effector of *Lmna*$^{-/-}$, *Lmna*Δ9, and LAΔ50 HGPS pathologies.

How does Sun1 overaccumulate in *Lmna*$^{-/-}$, *Lmna*Δ9, and LAΔ50 HGPS cells? Sun1 is normally located in the NE,

intensities less than 2-fold different from average are represented by blue bar; cells that are >2-fold, but <5fold are represented by pink bar; cells that stained >5-fold above average are represented by brown bar. *$p < 0.001$ when compared to AG03512 cells (t test).

(D) Quantification of the prevalence of cells from (B) with nuclear irregularities. ‡, $p < 0.0001$, when comparing the same cells treated with control RNAi or SUN1-RNAi (Fisher's exact test). See also Figure S5.

(E) Aberrant nuclear morphology in normal and HGPS fibroblasts transfected with an HA-tagged human SUN1 expression plasmid. Two hundred mock transfected cells per sample and fifty transfected cells per sample were scored. *P* values, Fisher's exact test.

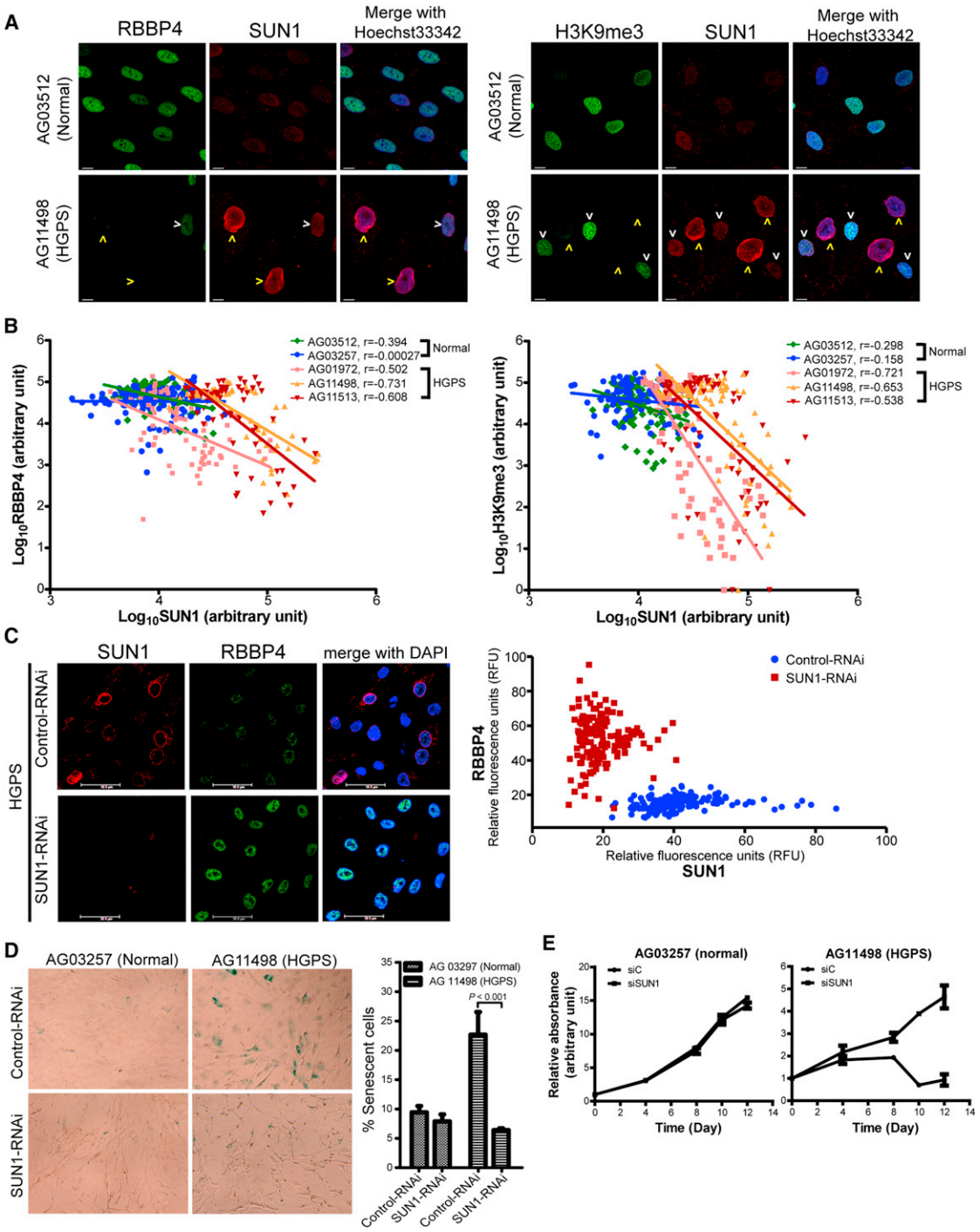

Figure 7. Knockdown of SUN1 Alleviated HGPS-Associated Loss of NURD Complex and Cellular Senescence

(A) Normal (AG03512) and HGPS (AG11498) skin fibroblasts were stained for heterochromatin markers (RBBP4 or H3K9me3; green) and SUN1 (red). Yellow arrowheads point to high-SUN1 cells; white arrowheads denote low-SUN1 cells. See also Figure S6.

(B) Expression levels of RBBP4 or H3K9me3 and SUN1 in two normal and three HGPS skin fibroblasts were quantified by MetaMorph software. Each dot represents fluorescence intensity (in Log_{10} scale) in a single cell of RBBP4 (left) or H3K9me3 (right) versus SUN1. Linear curve fitting and correlation coefficient (r) are indicated. In HGPS cells, RBBP4 and H3K9me3 expression correlates negatively with SUN1 expression.

(C) HGPS fibroblasts (AG03513) treated with control or SUN1 siRNA for 72 hr were stained with antibodies for SUN1 (red) and RBBP4 (green). Increased RBBP4 expression was observed in SUN1 siRNA-treated cells compared to control siRNA-treated cells. Graphic quantification of the staining intensities of RBBP4 versus SUN1 in individual HGPS fibroblasts treated with control (blue) or SUN1 (brown) siRNA is shown (right); each dot represents a single cell (154 control and 157 SUN1 RNAi treated cells were quantified).

positioned by mechanisms that are still obscure but may depend on interaction with lamin A filaments underlying the nuclear matrix (Haque et al., 2006; Mattioli et al., 2011; Ostlund et al., 2009). As noted above, a SUN1 protein deleted in its N-terminal (~100 amino acids) lamin A-interacting domain relocates from the NE to the Golgi (Figure S4; Haque et al., 2010; Chi et al., 2007). Emerging evidence suggests that the SUN1-related SUN2 protein has a Golgi retrieval sequence (Turgay et al., 2010) that is required for retrieval of SUN2 from the Golgi to the ER. Differences between the two proteins may explain why Sun1, but not Sun2, expressed in the absence of cell endogenous lamin A (i.e., *Lmna*$^{-/-}$ cells; Figure 3 and Figure S2), accumulates in the Golgi. Our findings show that Sun1 accumulation arises from reduced protein turnover (Figure S3) and not increased transcription (Figures S2F and S5C), suggesting that approaches to enhance protein degradation might be therapeutically beneficial (Cao et al., 2011).

We did not discern obvious Golgi overaccumulation of endogenous SUN1 in LAΔ50 HGPS cells. Although the explanation for this remains unclear, it could be that Golgi overaccumulation of SUN1 in human cells is highly toxic and selects rapidly against the viability of cultured HGPS cells, or that the heterozygous expression of wild-type lamin A in LAΔ50 HGPS cells is sufficient to locate endogenous SUN1 to the NE, preventing overt Golgi misaccumulation. Relevant to the former explanation, we observed that early-passage *Lmna*$^{-/-}$ MEFs show more dramatic Sun1-Golgi misaccumulation than late-passage counterparts, consistent with selection against cells with high Sun1-Golgi misaccumulation.

What might be the consequences of Sun1 mislocation in the Golgi? Our Golgi-targeting experiments with mSun1-Tgn38 (Figure 4) and SUN1 (103–785) mutant protein (Figure S4) showed that Golgi storage of Sun1 is cytotoxic. This toxicity may be akin to that elicited in abnormal human lysosomal (Metz et al., 2011) or ER storage (Rutishauser and Spiess, 2002) diseases. Aside from organelle storage disorders, other types of protein aggregation maladies like Alzheimer's (Gouras et al., 2010) exist. In Alzheimer's disease, evidence now suggests that it is the small, soluble amyloid-β oligomers, not the large, easily visualized amyloid-β fibrils/plaques, that produce neurotoxicity (Crews and Masliah, 2010). As mentioned above, we currently do not exclude that Golgi accumulation of SUN1 may indeed occur in LAΔ50 HGPS cells in vivo and that such cells may have rapidly succumbed and therefore are not represented in the mostly late-passage repository-deposited HGPS fibroblasts (Table S1). However, like soluble amyloid-β oligomers, which need not present as gross aggregates to be cytotoxic, it may be that the degree of SUN1 overexpression in LAΔ50 HGPS cells (Figure 6E) is sufficient to functionally trigger pathology without having to reach levels required for overt Golgi spillage. In LAΔ50 HGPS cells, increased SUN1 accumulation in the nuclear envelope may sufficiently create dysfunction by rendering a more rigid meshwork.

Progerin underlies LAΔ50 HGPS disease development (Eriksson et al., 2003; Scaffidi and Misteli, 2005; Goldman et al., 2004). How does SUN1 fit into the picture where progerin synthesis is the initial event inciting cellular dysfunction? In primary LAΔ50 HGPS cells or *Lmna*Δ9 mice where progerin (Figure S5B) or lamin A-ΔExon9 protein is expressed, Sun1 knockdown is sufficient to remedy cellular aberrancies and also senescence and longevity defects (Figures 1, 6, and 7). A cogent interpretation of these results is that SUN1 accumulation is positioned downstream of progerin or lamin A-ΔExon9, such that the depletion of SUN1 sufficiently interrupts pathologic signaling. In *Lmna*$^{-/-}$ mice, in which no progerin protein is synthesized, our data show that Sun1 accumulation remains an important trigger of loss-of-lamin A pathology. Future experiments are needed to clarify, in noncodon 1824 (i.e., non LAΔ50) forms of HGPS (Plasilova et al., 2004) and in the many rare dystrophic human diseases (Burke et al., 2001; Chi et al., 2009a; Capell and Collins, 2006; Kudlow et al., 2007) where no gain-of-function progerin-like protein is synthesized, whether SUN1 (or other nuclear envelope protein) misaccumulation is similarly important to pathogenesis. Our current findings do suggest that at least in the *Lmna*$^{-/-}$, *Lmna*Δ9, and LAΔ50 HGPS diseases, Sun1 overaccumulation is critical to pathologies. If this notion can be broadly applied, it suggests that future clinical trials and therapies for laminopathies that treat disease upstream events (i.e., targeting progerin) without resolving the downstream pathogenic events (i.e., Sun1 misaccumulation) may be ineffective.

EXPERIMENTAL PROCEDURES

Animals

Knockout mice were created using standard procedures. Because *Sun1*$^{-/-}$ and *Lmna*$^{-/-}$ mice are reproductively defective (Ding et al., 2007; Alsheimer et al., 2004; Chi et al., 2009b), *Sun1*$^{+/-}$ mice were crossed with *Lmna*$^{+/-}$ mice to generate *Lmna*$^{-/-}$*Sun1*$^{-/-}$ mice, or *Sun1*$^{+/-}$ mice were crossed with *Lmna*$^{L530P/+}$ mice (Mounkes et al., 2003) to generate *Lmna*Δ9*Sun1*$^{-/-}$ mice. *Lmna* mutant lines are available from Jax Labs and *Lmna*Δ9 mice from C.L. Stewart. Mouse genotypes were verified by PCR. All animal experiments were conducted according to animal study protocols approved by the National Institutes of Health (NIH) or the Singapore Animal Use Committee.

Immunofluorescence and Confocal Microscopy

Cells, fixed in 4% paraformaldehyde in PBS for 30 min and permeabilized with 0.1% Triton X-100 for 5 min at room temperatures, were incubated with 1% BSA in PBS for 30 min to block nonspecific binding. Antibodies were diluted at 1:100 to 1:1,000 and incubated for 1.5 hr at room temperature. After three washes with PBS, cells were probed with fluorescent (Alexa-488, Alexa-594, or Alexa-647)-conjugated secondary antibodies. Nuclei were counterstained with Hoechst33342 or DAPI (Invitrogen), and Sun1 intensity was visualized

(D) Visualization (left) and quantification (right) of acidic senescence associated β-galactosidase (SA-β-Gal) in normal (AG03257) and HGPS (AG11498 at passage 8) fibroblasts transfected with control or SUN1 RNAi for 96 hr. Standard deviations are from three independent assays counting 1200 to 2000 cells in each experiment. Cell scoring was performed in a blinded fashion by an independent investigator. P value (Chi-square) is indicated.

(E) Cell proliferation in normal (AG03257) and HGPS (AG11498) cells transfected with control or SUN1 RNAi. Cells at ~50% confluency were transfected. When cells reached confluency, equal numbers were seeded into dishes and quantified for proliferation using Cell Counting Kit-8 24 hr after cell seeding (day 0) and after another 4, 8, 10, and 12 days. Relative absorbance at 460 nm was obtained by [(Absorbance$_{460nm}$-background Absorbance$_{460nm}$) at day N]/[(Absorbance$_{460nm}$-background Absorbance$_{460nm}$) at day 0]. Standard deviations are from triplicate experiments.

using a Leica TCS SP5 microscope and quantified by the ImageJ 1.42q (NIH) or MetaMorph (Molecular Devices) software. Other procedures are in Extended Experimental Procedures.

SUPPLEMENTAL INFORMATION

Supplemental Information includes Extended Experimental Procedures, six figures, and one table and can be found with this article online at doi:10.1016/j.cell.2012.01.059.

ACKNOWLEDGMENTS

Work was supported by NIAID intramural funds, the IATAP, NIAID contract to SoBran, Inc., the NHRI, Taiwan (NHRI 99A1-CSPP11-014), and NSC, Taiwan (NSC 98-2320-B-400-009-MY3), and the Singapore Biomedical Research Council and Agency for Science, Technology and Research (A*STAR). We thank S.-Y. Chuang, E. Miyagi, J.M. Ward, L.I. Cheng, Z.J. Chen, J. Kabat, S. Becker, S. Bradford, Q. Su, and D. Donahue for assistance; and W. Leonard, J. Hanover, A. Dayton, Y.B. Shi, and D. Camerini-Otero for reading the manuscript.

Received: August 22, 2011
Revised: December 1, 2011
Accepted: January 30, 2012
Published: April 26, 2012

REFERENCES

Alsheimer, M., Liebe, B., Sewell, L., Stewart, C.L., Scherthan, H., and Benavente, R. (2004). Disruption of spermatogenesis in mice lacking A-type lamins. J. Cell Sci. *117*, 1173–1178.

Bonne, G., Di Barletta, M.R., Varnous, S., Bécane, H.M., Hammouda, E.H., Merlini, L., Muntoni, F., Greenberg, C.R., Gary, F., Urtizberea, J.A., et al. (1999). Mutations in the gene encoding lamin A/C cause autosomal dominant Emery-Dreifuss muscular dystrophy. Nat. Genet. *21*, 285–288.

Burke, B., and Stewart, C.L. (2002). Life at the edge: the nuclear envelope and human disease. Nat. Rev. Mol. Cell Biol. *3*, 575–585.

Burke, B., and Stewart, C.L. (2006). The laminopathies: the functional architecture of the nucleus and its contribution to disease. Annu. Rev. Genomics Hum. Genet. *7*, 369–405.

Burke, B., Mounkes, L.C., and Stewart, C.L. (2001). The nuclear envelope in muscular dystrophy and cardiovascular diseases. Traffic *2*, 675–683.

Burtner, C.R., and Kennedy, B.K. (2010). Progeria syndromes and ageing: what is the connection? Nat. Rev. Mol. Cell Biol. *11*, 567–578.

Cao, H., and Hegele, R.A. (2000). Nuclear lamin A/C R482Q mutation in Canadian kindreds with Dunnigan-type familial partial lipodystrophy. Hum. Mol. Genet. *9*, 109–112.

Cao, K., Graziotto, J.J., Blair, C.D., Mazzulli, J.R., Erdos, M.R., Krainc, D., and Collins, F.S. (2011). Rapamycin reverses cellular phenotypes and enhances mutant protein clearance in Hutchinson-Gilford progeria syndrome cells. Sci. Transl. Med. *3*, 89ra58.

Capell, B.C., and Collins, F.S. (2006). Human laminopathies: nuclei gone genetically awry. Nat. Rev. Genet. *7*, 940–952.

Chaouch, M., Allal, Y., De Sandre-Giovannoli, A., Vallat, J.M., Amer-el-Khedoud, A., Kassouri, N., Chaouch, A., Sindou, P., Hammadouche, T., Tazir, M., et al. (2003). The phenotypic manifestations of autosomal recessive axonal Charcot-Marie-Tooth due to a mutation in Lamin A/C gene. Neuromuscul. Disord. *13*, 60–67.

Chen, L., Lee, L., Kudlow, B.A., Dos Santos, H.G., Sletvold, O., Shafeghati, Y., Botha, E.G., Garg, A., Hanson, N.B., Martin, G.M., et al. (2003). LMNA mutations in atypical Werner's syndrome. Lancet *362*, 440–445.

Chi, Y.H., Haller, K., Peloponese, J.M., Jr., and Jeang, K.T. (2007). Histone acetyltransferase hALP and nuclear membrane protein hsSUN1 function in de-condensation of mitotic chromosomes. J. Biol. Chem. *282*, 27447–27458.

Chi, Y.H., Chen, Z.J., and Jeang, K.T. (2009a). The nuclear envelopathies and human diseases. J. Biomed. Sci. *16*, 96.

Chi, Y.H., Cheng, L.I., Myers, T., Ward, J.M., Williams, E., Su, Q., Faucette, L., Wang, J.Y., and Jeang, K.T. (2009b). Requirement for Sun1 in the expression of meiotic reproductive genes and piRNA. Development *136*, 965–973.

Crews, L., and Masliah, E. (2010). Molecular mechanisms of neurodegeneration in Alzheimer's disease. Hum. Mol. Genet. *19*(R1), R12–R20.

Crisp, M., Liu, Q., Roux, K., Rattner, J.B., Shanahan, C., Burke, B., Stahl, P.D., and Hodzic, D. (2006). Coupling of the nucleus and cytoplasm: role of the LINC complex. J. Cell Biol. *172*, 41–53.

De Sandre-Giovannoli, A., Chaouch, M., Kozlov, S., Vallat, J.M., Tazir, M., Kassouri, N., Szepetowski, P., Hammadouche, T., Vandenberghe, A., Stewart, C.L., et al. (2002). Homozygous defects in LMNA, encoding lamin A/C nuclear-envelope proteins, cause autosomal recessive axonal neuropathy in human (Charcot-Marie-Tooth disorder type 2) and mouse. Am. J. Hum. Genet. *70*, 726–736.

De Sandre-Giovannoli, A., Bernard, R., Cau, P., Navarro, C., Amiel, J., Boccaccio, I., Lyonnet, S., Stewart, C.L., Munnich, A., Le Merrer, M., and Lévy, N. (2003). Lamin a truncation in Hutchinson-Gilford progeria. Science *300*, 2055.

DeBusk, F.L. (1972). The Hutchinson-Gilford progeria syndrome. Report of 4 cases and review of the literature. J. Pediatr. *80*, 697–724.

Di Micco, R., Sulli, G., Dobreva, M., Liontos, M., Botrugno, O.A., Gargiulo, G., dal Zuffo, R., Matti, V., d'Ario, G., Montani, E., et al. (2011). Interplay between oncogene-induced DNA damage response and heterochromatin in senescence and cancer. Nat. Cell Biol. *13*, 292–302.

Ding, X., Xu, R., Yu, J., Xu, T., Zhuang, Y., and Han, M. (2007). SUN1 is required for telomere attachment to nuclear envelope and gametogenesis in mice. Dev. Cell *12*, 863–872.

Eriksson, M., Brown, W.T., Gordon, L.B., Glynn, M.W., Singer, J., Scott, L., Erdos, M.R., Robbins, C.M., Moses, T.Y., Berglund, P., et al. (2003). Recurrent de novo point mutations in lamin A cause Hutchinson-Gilford progeria syndrome. Nature *423*, 293–298.

Goldman, R.D., Shumaker, D.K., Erdos, M.R., Eriksson, M., Goldman, A.E., Gordon, L.B., Gruenbaum, Y., Khuon, S., Mendez, M., Varga, R., and Collins, F.S. (2004). Accumulation of mutant lamin A causes progressive changes in nuclear architecture in Hutchinson-Gilford progeria syndrome. Proc. Natl. Acad. Sci. USA *101*, 8963–8968.

Gouras, G.K., Tampellini, D., Takahashi, R.H., and Capetillo-Zarate, E. (2010). Intraneuronal beta-amyloid accumulation and synapse pathology in Alzheimer's disease. Acta Neuropathol. *119*, 523–541.

Güttinger, S., Laurell, E., and Kutay, U. (2009). Orchestrating nuclear envelope disassembly and reassembly during mitosis. Nat. Rev. Mol. Cell Biol. *10*, 178–191.

Haque, F., Lloyd, D.J., Smallwood, D.T., Dent, C.L., Shanahan, C.M., Fry, A.M., Trembath, R.C., and Shackleton, S. (2006). SUN1 interacts with nuclear lamin A and cytoplasmic nesprins to provide a physical connection between the nuclear lamina and the cytoskeleton. Mol. Cell. Biol. *26*, 3738–3751.

Haque, F., Mazzeo, D., Patel, J.T., Smallwood, D.T., Ellis, J.A., Shanahan, C.M., and Shackleton, S. (2010). Mammalian SUN protein interaction networks at the inner nuclear membrane and their role in laminopathy disease processes. J. Biol. Chem. *285*, 3487–3498.

Hernandez, L., Roux, K.J., Wong, E.S., Mounkes, L.C., Mutalif, R., Navasankari, R., Rai, B., Cool, S., Jeong, J.W., Wang, H., et al. (2010). Functional coupling between the extracellular matrix and nuclear lamina by Wnt signaling in progeria. Dev. Cell *19*, 413–425.

Kitaguchi, T., Matsubara, S., Sato, M., Miyamoto, K., Hirai, S., Schwartz, K., and Bonne, G. (2001). A missense mutation in the exon 8 of lamin A/C gene in a Japanese case of autosomal dominant limb-girdle muscular dystrophy and cardiac conduction block. Neuromuscul. Disord. *11*, 542–546.

Kudlow, B.A., Kennedy, B.K., and Monnat, R.J., Jr. (2007). Werner and Hutchinson-Gilford progeria syndromes: mechanistic basis of human progeroid diseases. Nat. Rev. Mol. Cell Biol. *8*, 394–404.

Lei, K., Zhang, X., Ding, X., Guo, X., Chen, M., Zhu, B., Xu, T., Zhuang, Y., Xu, R., and Han, M. (2009). SUN1 and SUN2 play critical but partially redundant roles in anchoring nuclei in skeletal muscle cells in mice. Proc. Natl. Acad. Sci. USA *106*, 10207–10212.

Liu, B., Wang, J., Chan, K.M., Tjia, W.M., Deng, W., Guan, X., Huang, J.D., Li, K.M., Chau, P.Y., Chen, D.J., et al. (2005). Genomic instability in laminopathy-based premature aging. Nat. Med. *11*, 780–785.

Malone, C.J., Fixsen, W.D., Horvitz, H.R., and Han, M. (1999). UNC-84 localizes to the nuclear envelope and is required for nuclear migration and anchoring during C. elegans development. Development *126*, 3171–3181.

Marie, M., Sannerud, R., Avsnes Dale, H., and Saraste, J. (2008). Take the 'A' train: on fast tracks to the cell surface. Cell. Mol. Life Sci. *65*, 2859–2874.

Mattioli, E., Columbaro, M., Capanni, C., Maraldi, N.M., Cenni, V., Scotlandi, K., Marino, M.T., Merlini, L., Squarzoni, S., and Lattanzi, G. (2011). Prelamin A-mediated recruitment of SUN1 to the nuclear envelope directs nuclear positioning in human muscle. Cell Death Differ. *18*, 1305–1315.

Merideth, M.A., Gordon, L.B., Clauss, S., Sachdev, V., Smith, A.C., Perry, M.B., Brewer, C.C., Zalewski, C., Kim, H.J., Solomon, B., et al. (2008). Phenotype and course of Hutchinson-Gilford progeria syndrome. N. Engl. J. Med. *358*, 592–604.

Metz, T.F., Mechtler, T.P., Orsini, J.J., Martin, M., Shushan, B., Herman, J.L., Ratschmann, R., Item, C.B., Streubel, B., Herkner, K.R., and Kasper, D.C. (2011). Simplified newborn screening protocol for lysosomal storage disorders. Clin. Chem. *57*, 1286–1294.

Mounkes, L.C., Kozlov, S., Hernandez, L., Sullivan, T., and Stewart, C.L. (2003). A progeroid syndrome in mice is caused by defects in A-type lamins. Nature *423*, 298–301.

Muchir, A., Bonne, G., van der Kooi, A.J., van Meegen, M., Baas, F., Bolhuis, P.A., de Visser, M., and Schwartz, K. (2000). Identification of mutations in the gene encoding lamins A/C in autosomal dominant limb girdle muscular dystrophy with atrioventricular conduction disturbances (LGMD1B). Hum. Mol. Genet. *9*, 1453–1459.

Nagano, A., and Arahata, K. (2000). Nuclear envelope proteins and associated diseases. Curr. Opin. Neurol. *13*, 533–539.

Novelli, G., Muchir, A., Sangiuolo, F., Helbling-Leclerc, A., D'Apice, M.R., Massart, C., Capon, F., Sbraccia, P., Federici, M., Lauro, R., et al. (2002). Mandibuloacral dysplasia is caused by a mutation in LMNA-encoding lamin A/C. Am. J. Hum. Genet. *71*, 426–431.

Ostlund, C., Folker, E.S., Choi, J.C., Gomes, E.R., Gundersen, G.G., and Worman, H.J. (2009). Dynamics and molecular interactions of linker of nucleoskeleton and cytoskeleton (LINC) complex proteins. J. Cell Sci. *122*, 4099–4108.

Pegoraro, G., Kubben, N., Wickert, U., Göhler, H., Hoffmann, K., and Misteli, T. (2009). Ageing-related chromatin defects through loss of the NURD complex. Nat. Cell Biol. *11*, 1261–1267.

Plasilova, M., Chattopadhyay, C., Pal, P., Schaub, N.A., Buechner, S.A., Mueller, H., Miny, P., Ghosh, A., and Heinimann, K. (2004). Homozygous missense mutation in the lamin A/C gene causes autosomal recessive Hutchinson-Gilford progeria syndrome. J. Med. Genet. *41*, 609–614.

Rutishauser, J., and Spiess, M. (2002). Endoplasmic reticulum storage diseases. Swiss Med. Wkly. *132*, 211–222.

Scaffidi, P., and Misteli, T. (2005). Reversal of the cellular phenotype in the premature aging disease Hutchinson-Gilford progeria syndrome. Nat. Med. *11*, 440–445.

Shimi, T., Pfleghaar, K., Kojima, S., Pack, C.G., Solovei, I., Goldman, A.E., Adam, S.A., Shumaker, D.K., Kinjo, M., Cremer, T., and Goldman, R.D. (2008). The A- and B-type nuclear lamin networks: microdomains involved in chromatin organization and transcription. Genes Dev. *22*, 3409–3421.

Shumaker, D.K., Dechat, T., Kohlmaier, A., Adam, S.A., Bozovsky, M.R., Erdos, M.R., Eriksson, M., Goldman, A.E., Khuon, S., Collins, F.S., et al. (2006). Mutant nuclear lamin A leads to progressive alterations of epigenetic control in premature aging. Proc. Natl. Acad. Sci. USA *103*, 8703–8708.

Stewart, C.L., Roux, K.J., and Burke, B. (2007). Blurring the boundary: the nuclear envelope extends its reach. Science *318*, 1408–1412.

Stuurman, N., Heins, S., and Aebi, U. (1998). Nuclear lamins: their structure, assembly, and interactions. J. Struct. Biol. *122*, 42–66.

Sullivan, T., Escalante-Alcalde, D., Bhatt, H., Anver, M., Bhat, N., Nagashima, K., Stewart, C.L., and Burke, B. (1999). Loss of A-type lamin expression compromises nuclear envelope integrity leading to muscular dystrophy. J. Cell Biol. *147*, 913–920.

Szentpetery, Z., Várnai, P., and Balla, T. (2010). Acute manipulation of Golgi phosphoinositides to assess their importance in cellular trafficking and signaling. Proc. Natl. Acad. Sci. USA *107*, 8225–8230.

Thyberg, J., and Moskalewski, S. (1999). Role of microtubules in the organization of the Golgi complex. Exp. Cell Res. *246*, 263–279.

Turgay, Y., Ungricht, R., Rothballer, A., Kiss, A., Csucs, G., Horvath, P., and Kutay, U. (2010). A classical NLS and the SUN domain contribute to the targeting of SUN2 to the inner nuclear membrane. EMBO J. *29*, 2262–2275.

Worman, H.J., and Courvalin, J.C. (2004). How do mutations in lamins A and C cause disease? J. Clin. Invest. *113*, 349–351.

Yu, J., Lei, K., Zhou, M., Craft, C.M., Xu, G., Xu, T., Zhuang, Y., Xu, R., and Han, M. (2011). KASH protein Syne-2/Nesprin-2 and SUN proteins SUN1/2 mediate nuclear migration during mammalian retinal development. Hum. Mol. Genet. *20*, 1061–1073.

Zhang, X., Lei, K., Yuan, X., Wu, X., Zhuang, Y., Xu, T., Xu, R., and Han, M. (2009). SUN1/2 and Syne/Nesprin-1/2 complexes connect centrosome to the nucleus during neurogenesis and neuronal migration in mice. Neuron *64*, 173–187.

EXTENDED EXPERIMENTAL PROCEDURES

Cell Culture

Normal (AG03512, AG03257, AG03258, AG08469) and HGPS (AG01972, AG06297, AG11498, AG11513, AG06917, AG03513, AG03198) human skin fibroblasts were from the National Institute of Aging (NIA) Aged Cell Repository distributed by the Coriell Institute. Cells were maintained in high glucose MEM containing 10%–15% FBS and supplemented with 2 mM L-glutamine, 1 mM sodium pyruvate and antibiotics. Mouse embryonic fibroblasts (MEFs) were prepared from E15.5 embryos. Cells were dissociated by trypsin and were maintained in Dulbecco's modified eagle medium (DMEM) supplemented with 15% fetal bovine serum (FBS), 2 mM L-glutamine and antibiotics.

Plasmids

The mouse Sun1 (mSun1, accession number: NM_024451, 913 a. a.), mSun1-FLAG, mSun1-Tgn38-HA, full length human SUN1 (hSUN1-HA, accession number: NM_001130965, 785 aa), hSUN1 (aa 103–785)-HA and mouse lamin A expression plasmids were constructed based on the pcDNA3.1 vector (Invitrogen). All the constructs generated were verified by DNA sequencing, and the expression of the cloned genes was confirmed by western analyses. Lipofectamine 2000 (Invitrogen) and PolyJet (SignaGen Laboratories) were used for plasmid transfections.

Reagents, Primers, and RT-PCR

Regents were obtained from the following resources. Sigma-Aldrich: nocodazole (M1404), lactacystin (L6785), brefeldin A (BFA, B5936), latrunculin B (LAT-B, L5288), cycloheximide (C4859). Primer sequences for *Sun1* genotyping: 5′-GGCAAGTGGAT CTCTTGTGAATTCTTGAC-3′ and 5′-GTAGCACCCACCTTGGTGAGCTGGTAC-3′. WT mice produced a 1262 bp fragment and the *Sun1* knockout mice produced a 263 bp fragment. Primer sequences for *Lmna* genotyping: common forward primer for WT and *Lmna* KO 5′-AGTTCGTGCGGCTGCGCAACAAGTCCAACG-3′; reverse primer for WT: 5′-GTCATCAAAGGATCGTCACCATTCT GAC-3′; reverse primer for *Lmna* KO: 5′-CCATTCGACCACCAAGCGAAACATCGC-3′. Wild-type mice produced a 500 bp fragment and the *Lmna* knockout mice produced an 850 bp fragment.

For RT-PCR, total RNA was extracted from MEFs using TRIzol (Invitrogen). Complementary DNA (cDNA) was produced from MEFs RNA (5 μg) using the SuperScript II Reverse Transcriptase Kit (Invitrogen). Three pairs of primer p177/p178 (p177: 5′-GGGACAGC CAGGCTATTGATT; p178: 5′-CATGGCTTGTGCTCGAGGA), p1213/p1379 (p1213: 5′-CTTCTTACCAGGTGCCTTCG; p1379: 5′-GAA TCGTCCACCCTCTGTGT), and p140/p141 (p140: 5′-TATTGTGTCTGCCGTGAATC; p141: 5′-GCCGTCTTGGTCTCATAGGTC) (Ostlund et al., 2009) were used to amplify three coding regions of mouse Sun1, respectively. PCR products of mouse glyceraldehyde-3-phosphate dehydrogenase (Gapdh-F: 5′-TCACCACCATGGAGAAGGC; Gapdh-R: 5′-GCTAAGCAGTTGGTGGTGCA) were served as an internal control. Primers for RT-PCR of human *SUN1* (hsSUN1-F: 5′-GGACGTGTTTAAACCCACGACTT CTCG; hsSUN1-R: 5′-CTCTGACTTTAGCTGATCCAGCTCCAGC), human *GAPDH* (GAPDH-F: 5′-AGCCACATCGCTCAGACACC; GAPDH-R: 5′-GTACTCAGCGGCCAGCATCG).

Antibodies

The rabbit anti-SUN domain of mouse Sun1 (aa 701-913) was prepared as described in Chi et al. (2009b). Specificity of this antibody in western blot and immunofluorescence staining was examined and verified by comparing the signals from wild-type and *Sun1*$^{-/-}$ MEFs. The rabbit anti-human SUN1 antibody was prepared as described previously (Chi et al., 2007). Other antibodies were obtained from the following resources. Abcam: rabbit anti-GM130 (ab52649), rabbit anti-H3K9me3 (ab8898), rabbit anti-Sun2 (ab87036), mouse anti-RBBP4 (ab488); Sigma-Aldrich: mouse anti-αtubulin (T5168), mouse anti-Actin (A1978), mouse anti-HA (H3663), mouse anti-FLAG (F1804), rabbit anti-FLAG (F7425), rabbit anti-GM130 (G7295); Santa Cruz Biotechnology: mouse anti-lamin A/C (sc-7292), goat anti-lamin B1 (sc-6217), rabbit anti-Emerin (sc-15378); Covance: mouse anti-Nup153 (MMS-102P), mouse anti-human SUN1 (customized); Epitomics: rabbit anti-RBBP4 (2599-1). BD Transduction Laboratories: mouse anti-Calnexin (610524); mouse anti-GM130 (610823).

Western Blotting

To extract nuclear envelope proteins from human skin fibroblasts, cultured cells were washed twice with PBS. The cell pellet was incubated with ice-cold RIPA buffer [50 mM HEPES, pH 7.3, 150 mM NaCl, 2 mM EDTA, 20 mM β-gylcerophosphate, 0.1 mM Na_3VO_4, 1 mM NaF, 0.5 mM DTT and protease inhibitor cocktail (Roche)] containing 1% NP-40 and 1% SDS plus mild sonication. Lysates were then analyzed by 8% SDS-PAGE, transferred to polyvinylidene fluoride (PVDF, Millipore) membrane and blotted antibodies. Corresponding alkaline phosphatase-conjugated secondary antibodies (Sigma-Aldrich) were added, and the blots were developed by chemiluminescence following the manufacturer's protocol (Chemicon).

RNAi

Synthetic Stealth siRNA duplexes targeting human *SUN1* (5′-CCAUCCUGAGUAUACCUGUCUGUAU-3′) (Chi et al., 2007) were from Invitrogen. Small interfering RNAs were induced into human skin fibroblasts using the Lipofectamine 2000 transfection reagent (Invitrogen) or Lipofectamine RNAiMax trasnfection reagent (Invitrogen). For siRNA delivery using Lipofectamine 2000, 60 pmol of

siRNA mixed with 3 μl of Lipofectamine 2000 transfection reagent were used per well in a 12-well plate. For Lipofectamine RNAimax for siRNA delivery, only 3 pmol and 2 μl of the transfection reagent were used per well in a 12-well plate.

Golgi Fractionation

Golgi fractionation was performed using the Golgi isolation kit (Sigma-Aldrich, GL0010) according to the manufacturer's protocol with some modifications. Mouse liver was minced with 1 ml of 0.25 M sucrose isolation solution per 1 g of tissue. The tissue suspension was homogenized with six slow motions of the PTFE pestle at 300 rpm and centrifuged at 3,000 × g for 15 min at 4°C. Supernatant was transferred to a fresh tube and concentration of sucrose was adjusted to 1.25 M. A discontinuous gradient was built in an ultracentrifuge tube by adding 1.84 M sucrose solution, the sample (sucrose concentration adjusted to 1.25 M), 1.1 M sucrose solution and 0.25 M sucrose solution sequentially. After centrifugation at 12,000 × g for 3 hr, the Golgi-enriched fraction from the 1.1 M/0.25 M sucrose interphase was withdrawn and subjected to western analyses.

Senescence Assay

The senescence associated β-galactosidase (SA-β-Gal) assay was performed by following protocol of the Cellular Senescence Assay Kit from Cell Biolabs, Inc.

Cell Proliferation Assay

Cell proliferation was performed by quantifying viable cells with Cell Counting Kit-8 (Fluka) according to the manufacturer's protocol.

Micro-CT

Wild-type, *Sun1*$^{-/-}$, *Lmna*$^{-/-}$ and *Lmna*$^{-/-}$*Sun1*$^{-/-}$ mice were examined by compact cone-beam tomography (MicroCAT-II scanner). Whole-body scans were performed in the axial plane with the specimens mounted in a cylindrical sample holder. Micro-computed tomography (micro-CT) was performed at 55 kVp, with an anode current of 500 μA and a shutter speed of 500 ms. The femur bone specimens were fixed in 10% formalin buffered with phosphate and then examined by SkyScan 1172 Micro-CT. Three-dimensional images of the skeletons were reconstructed from the micro-CT scanning slices and used for analyses of the skeletal structure and morphology. Quantitative data were calculated by SkyScan CT-analyzer Software Guide. A manufacturer-provided hydroxyapatite phantom of known density was used to calibrate the mean density of bone volume and the cortical thickness.

MRI

Mouse cardiac magnetic resonance imaging (MRI) was conducted by following the NIH animal care and use guidelines. MRI experiments were performed in a 7.0T, 16-cm horizontal Bruker MR imaging system (Bruker) equipped with Bruker ParaVision 4.0 software. Mice were anesthesized with 1.5%–3% isoflurane and imaged with ECG, temperature and respiratory detection using a 38 mm Bruker birdcage volume coil. Magnevist (gadopentate dimeglumine contrast agent, Bayer HealthCare) diluted 1:10 with sterile 0.9% saline, was administered subcutaneously at 0.3 mmol Gd/kg. Intravenous route was not used due to small size of some mice (ca. 10-12 g) with invisible tail veins. T1 weighted gradient echo cine images of the heart were acquired in short axis from above the base to the apex (6-10 slices depending on slice thickness) with the following parameters: repetition time TR = 11 ms, echo time TE = 3.5 ms, 11 to 14 frames, 30 degree flip angle, 2.8 to 3.0 cm field of view, 256 × 256 matrix, respiratory and ECG-gated. 1.0 mm slice thickness with 4–5 averages was used on mice over 12 g and 0.75 mm thickness with 4-7 averages for mice less than 12 g. Cardiac MRI data were processed to determine ejection fractions and associated functional parameters using the CAAS-MRV-FARM software (Pie Medical Imaging, Netherlands.)

Statistics

Means and standard deviation are presented to describe the distribution. Student t test was used to compare mean difference between two groups. ANOVA analysis was performed to compare mean difference among groups. Multiple comparisons were carried out by Scheffe's Test. Kaplan-Meier method was used to draw the survival curves. Log-rank test was conducted on the homogeneity of survival curves among four types of mouse. We used Mixed model to compare the difference between body weight during the followed period among four types of mouse. We also used Generalized Estimating Equations (GEE) Method to compare the cell number among four types of MEF cells. The working correlation structure was set unstructured, and the linked function was set Poission distribution. Statistics were carried out by SAS 9.2 or GraphPad Prism 5.0.

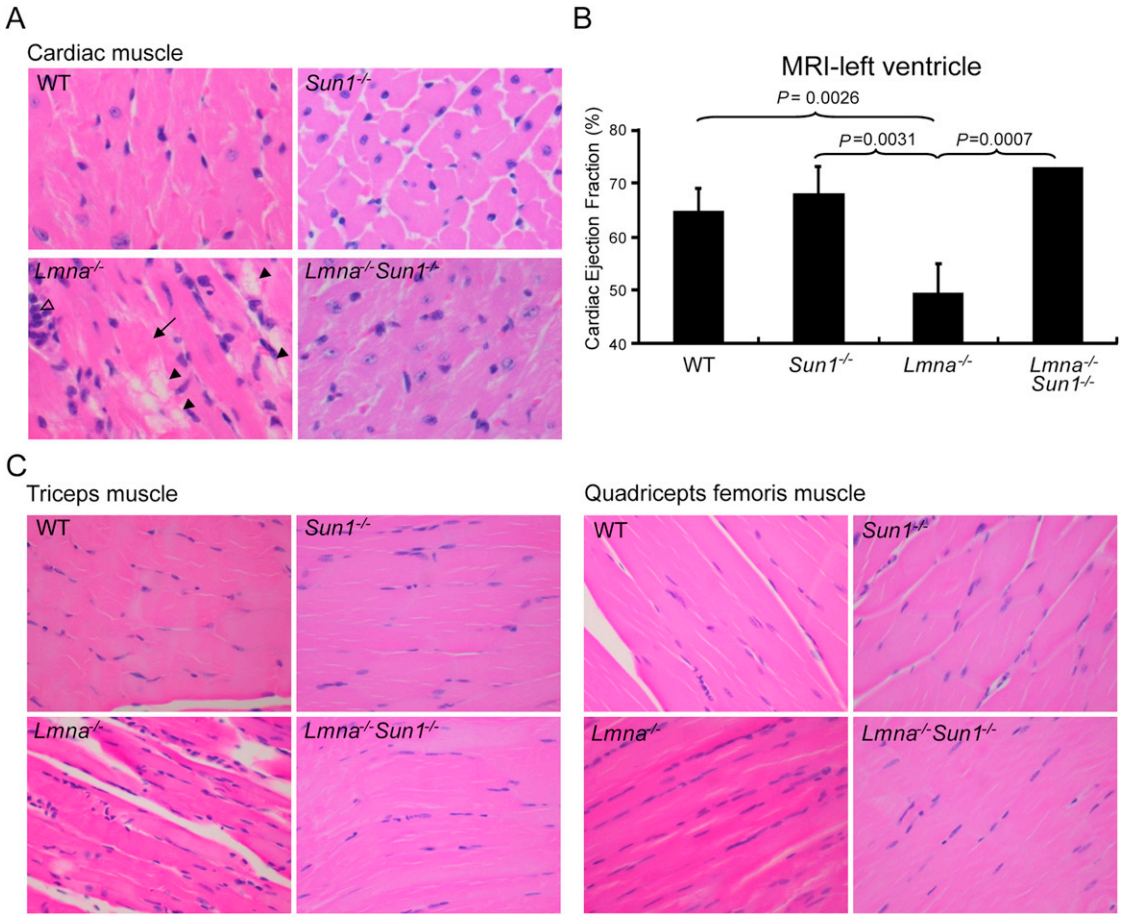

Figure S1. Multiple Tissue Defects in *Lmna*$^{-/-}$ Mice Are Ameliorated in *Lmna*$^{-/-}$*Sun1*$^{-/-}$ Double-Knockout Mice, Related to Figure 2

(A) Hematoxylin and eosin (H&E) -stained sections of tissues from 5–6 week old mice. In each case, *Lmna*$^{-/-}$*Sun1*$^{-/-}$ tissues are improved in pathology over *Lmna*$^{-/-}$ counterparts. Cardiac muscle: *Lmna*$^{-/-}$ cardiac muscle showed more tissue vacuoles than WT, *Sun1*$^{-/-}$, or *Lmna*$^{-/-}$*Sun1*$^{-/-}$ muscle (600 × magnifications). Hollow triangle: infiltrates of lymphocytes and neutrophils, solid triangle: sarcoplasmic vacuoles, arrow: myocyte necrosis.

(B) Cardiac function: Abnormal cardiovascular functions were found in the *Lmna*$^{-/-}$ mice; the left ventricle ejection fraction as indicated in the "Cardiovascular Parameters" was measured by MRI (magnetic resonance imaging). Values are mean ±SD.

(C) Tricep muscle and quadricep femoris muscle: the musculature of *Lmna*$^{-/-}$ mice contains smaller myocytes; the nuclei are closer together, and the myocytes adjacent to the bone are significantly atrophied (600 × magnifications).

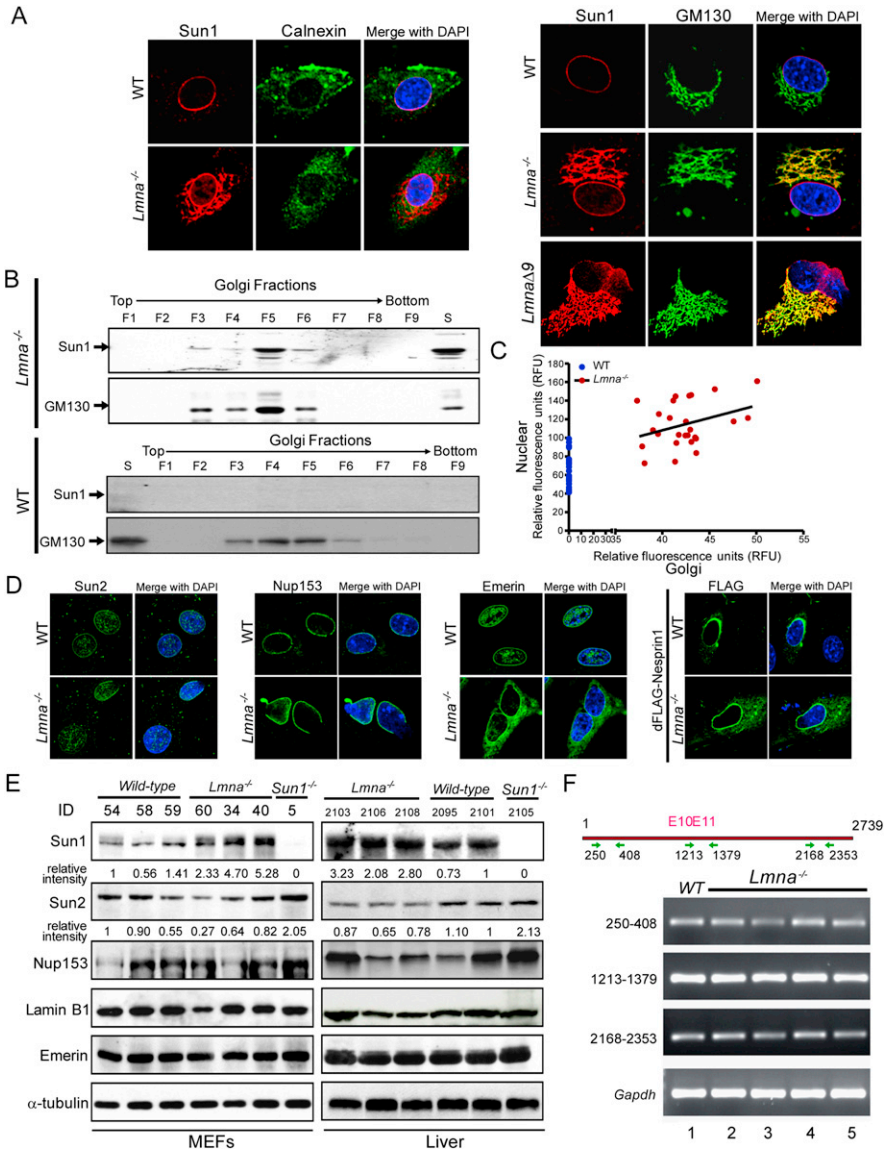

Figure S2. Loss of Lamin A Correlates with Sun1 Accumulation in the NE and Golgi, Related to Figure 3

(A) *Lmna*$^{-/-}$ MEFs or *Lmna*Δ9 MAFs (mouse adult fibroblasts) were stained with anti-Sun1 (red) and anti-GM130 (a Golgi marker; green; right middle panels) or anti-Calnexin (an ER marker; green; left middle panels). DAPI staining of DNA is in blue. Yellow in merged panels indicates Sun1 colocalization with GM130 in the Golgi, and absence of colocalization with Calnexin in the ER. Localization of Sun1 in the Golgi was observed in *Lmna*$^{-/-}$ and *Lmna*Δ9 cells. Images are summations of z-stacks.

(B) Golgi preparation using cytosolic lysate (S) from *Lmna*$^{-/-}$ liver tissue was fractionated on a sucrose density gradient; the Golgi fractions (F1–F9) were examined together and compared to total loading cytosolic lysate (S) by immunoblotting using anti-mouse Sun1 and anti-Golgi marker GM130, respectively. The mouse Sun1 protein cofractionated with Golgi constituent protein GM130. Golgi preparation from WT liver tissue fractionated in the same way is shown as control at the bottom. Unlike *Lmna*$^{-/-}$ liver cytosol, minimal Sun1 signal was detected in the WT cytosolic lysate (S).

(C) Correlation of Sun1 staining in the nucleus and Golgi in WT and *Lmna*$^{-/-}$ MEFs. Linear regression indicates a positive correlation (slope = 0.375) between Sun1 in the nucleus and in the Golgi in *Lmna*$^{-/-}$ MEFs.

(D) Confocal immunofluroscent localization of cell endogenous Sun2, Nup153, Emerin and transfected human Nesprin1 (accession number NM_133650, 982 aa) in WT and *Lmna*$^{-/-}$ MEFs. Nuclear envelope localization of Sun2 and Nup153 was not perturbed by *Lmna* depletion while some increased cytoplasmic distribution of Emerin and Nesprin1 was seen in *Lmna*$^{-/-}$ MEFs. No workable antibody that recognizes cell endogenous Nespirin1 was available; so the analysis was performed with FLAG-tagged transfected Nespirin1 stained with anti-FLAG.

(E) Western blotting of Sun1, Sun2, Nup153, lamin B1, Emerin and α-tubulin in MEFs (left) and mouse liver tissue (right). Wild-type, *Lmna*$^{-/-}$, and *Sun1*$^{-/-}$ samples were compared. Mouse identification (ID) numbers indicate individual animals. Aside from Sun1, no consistent difference was noted between *Lmna*$^{-/-}$ and WT cells or liver tissues.

(F) RT-PCR analysis of *Sun1* mRNA (nucleotides 250-408, 1213-1379 and 2168-2353) from wild-type (lane 1) and four individual *Lmna*$^{-/-}$ (lanes 2–5) MEFs. *Gapdh* is shown as control.

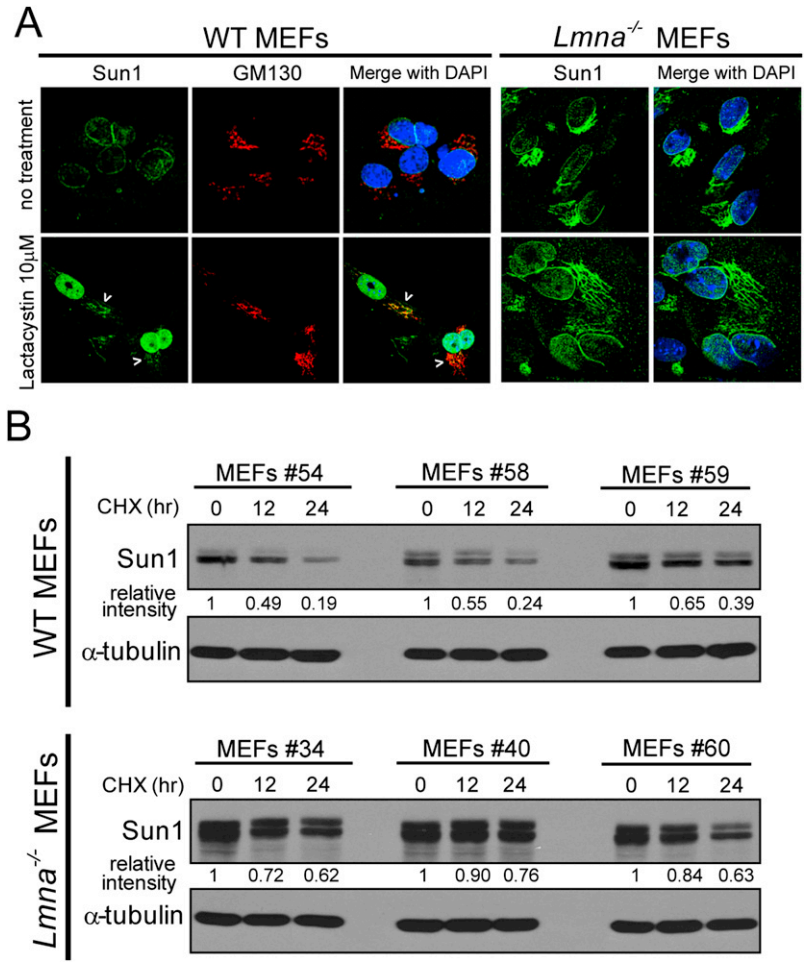

Figure S3. Analyses of Sun1 Protein Turnover, Related to Figure 3

(A) Immunofluorescence images of wild-type MEFs and *Lmna*$^{-/-}$ MEFs treated without or with 10 μM of lactacystin (for 14 hr). Cells were fixed and co-immunostained with rabbit anti-mSun1 (green) and mouse anti-GM130 (red) antibodies. DNA is in blue. Increased Sun1 is seen in the nucleus with some protein found in extranuclear locale of WT MEFs (in 10%–15% of cells, indicated by arrowheads) after lactacystin treatment. In lactacystin treated WT MEFs, Sun1 accumulation was observed in the nuclear membrane with a circumferential pattern and in the nucleoplasm with a punctate pattern. In *Lmna*$^{-/-}$ MEFs, Sun1 accumulation in the nucleus and in the Golgi is increased after lactacystin treatment.

(B) Western blotting of Sun1 in wild-type and *Lmna*$^{-/-}$ MEFs treated without or with 25 μg/ml cycloheximide (for 12 or 24 hr); α-tubulin was used as a normalization control. Relative amounts of Sun1 were calculated and shown in the numbers below the blot. The half life of the Sun1 protein is approximately 12 hr in WT MEFs and is calculated to approximate > 24 hr in *Lmna*$^{-/-}$ MEFs.

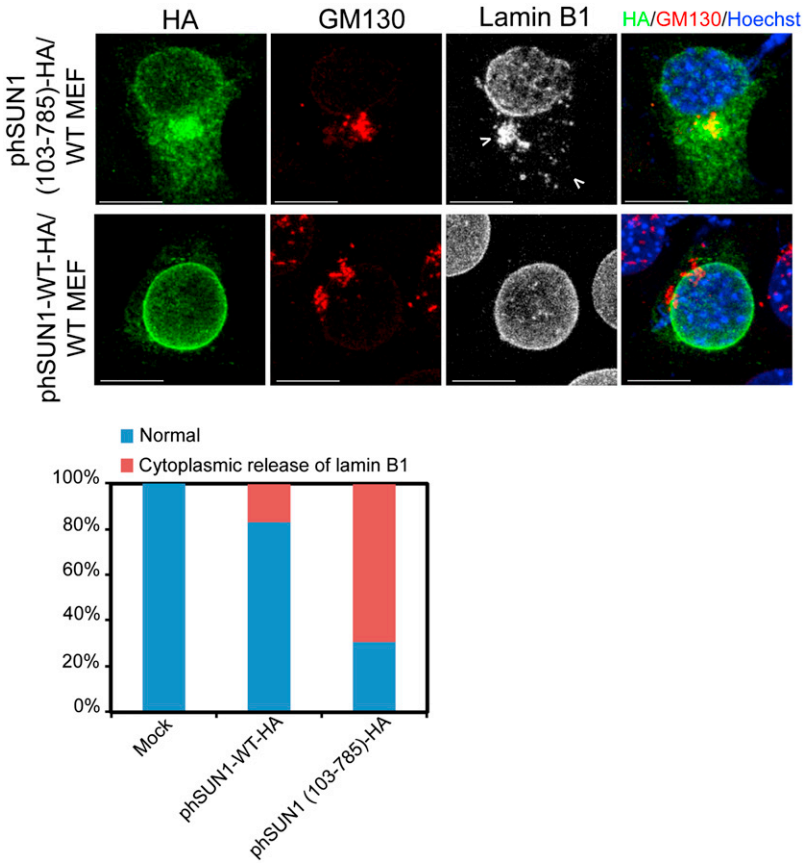

Figure S4. Human SUN1 Deleted for Its N-Terminal Lamin A-Interacting Domain Locates in the Golgi, Related to Figure 4

(Top) Localization of WT or N-terminal deletion (amino acids 103-785) mutant of HA-tagged human SUN1 in MEFs. Cells were co-immunostained with mouse anti-HA (green), rabbit anti-GM130 (red) and goat anti-lamin B1 (grayscale). DNA was stained with Hoechst33342 (blue). SUN1 (103-785) mutant protein localizes to extranuclear Golgi; while WT SUN1 is in the nuclear membrane. The arrowheads denote cytoplasmic lamin B1. Scale bars, 10 μm. (Bottom) Quantification of MEF cells with cytoplasmic release of lamin B1 in MEFs after 30 hr of transfection of HA-tagged wild-type human SUN1 or the SUN1 (103-785) mutant protein. One hundred cells were counted in each case.

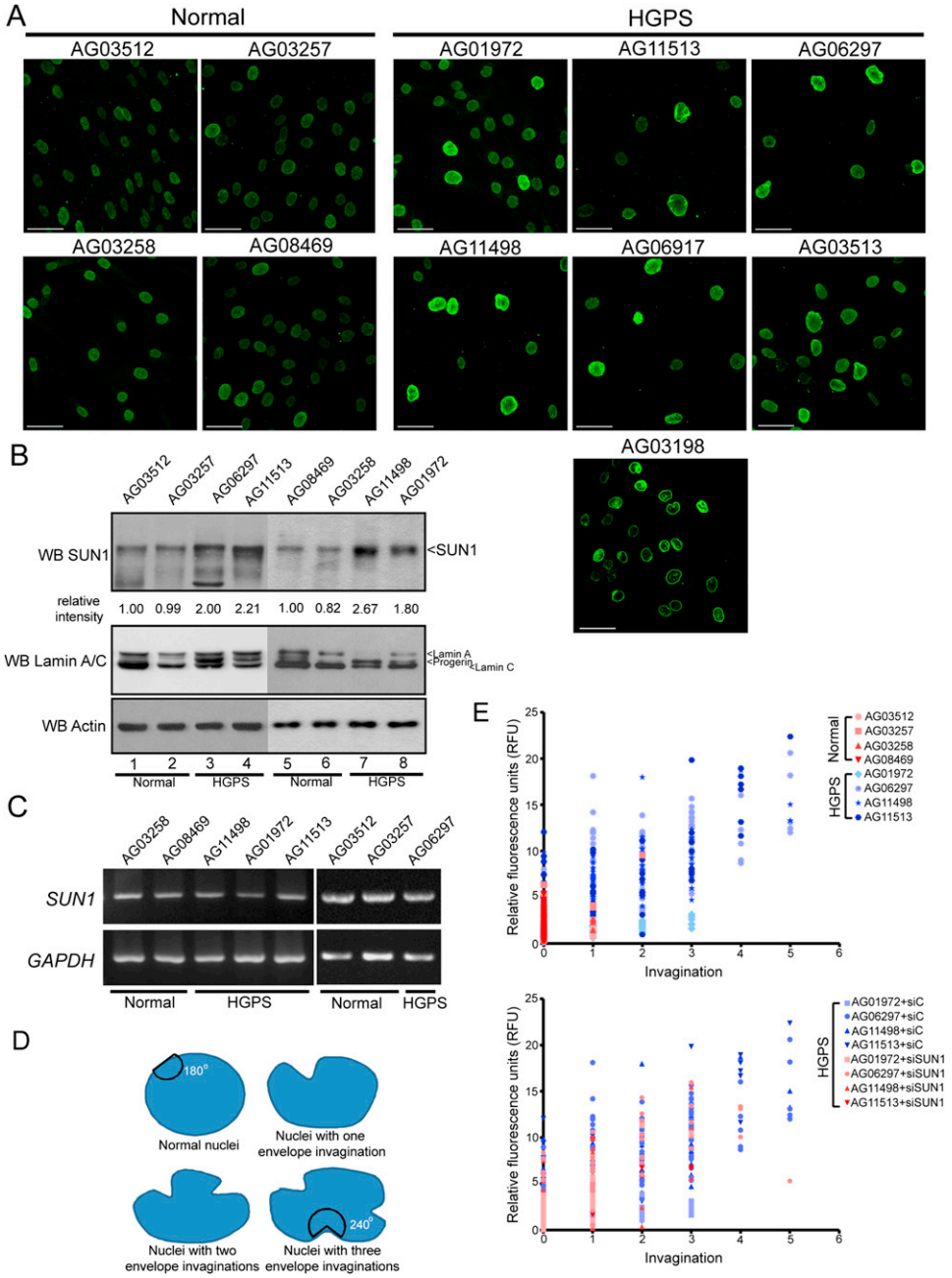

Figure S5. Properties of Normal Human and Hutchinson-Gilford Progeria Syndrome Skin Fibroblasts, Related to Figure 6

(A) Immunofluorescent SUN1 staining images of multiple cells from four normal (AG03512, AG03257, AG03258, AG08469) and seven HGPS (AG01972, AG11513, AG06297, AG11498, AG06917, AG11513, AG03198) fibroblasts (Table S1). Note that the increased expression of SUN1 is seen in all HGPS samples with one-third or more of cells in each HGPS visual field staining brightly green. Scale bars, 50 μm.

(B) Expression of SUN1, lamin A/C and progerin in normal and representative HGPS skin fibroblasts was assessed by western blotting. Progerin which is deleted for 50 amino acids from full length lamin A runs slightly faster in SDS-PAGE. Relative intensities of SUN1 expression levels compared to AG03512 (lanes 2-4) or AG08469 (lanes 6-8) are indicated in the numbers below the top panel.

(C) Expression of *SUN1* mRNA in normal and representative HGPS skin fibroblasts by RT-PCR. *GAPDH* was used for normalization.

(D) A cartoon of nuclei with shapes and contour changes that are scored as nuclear invaginations. Nuclei with > 240° contour changes are scored as aberrant invagination(s).

(E) Distribution of nuclear invaginations in normal and HGPS skin fibroblasts (as presented in Figures 5B–5D) treated with control (siC) or SUN1 siRNA (siSUN1). Significantly higher numbers of aberrant nuclear invaginations ($p < 0.001$) were seen for each of the HGPS cells compared to control AG03512 (normal skin fibroblasts, t test); similarly, significantly lower numbers of nuclear invaginations ($p < 0.0001$) were seen for all HGPS cells treated with SUN1-RNAi compare to Control-RNAi treated cells (t test). RFU are relative fluorescent units of staining for SUN1.

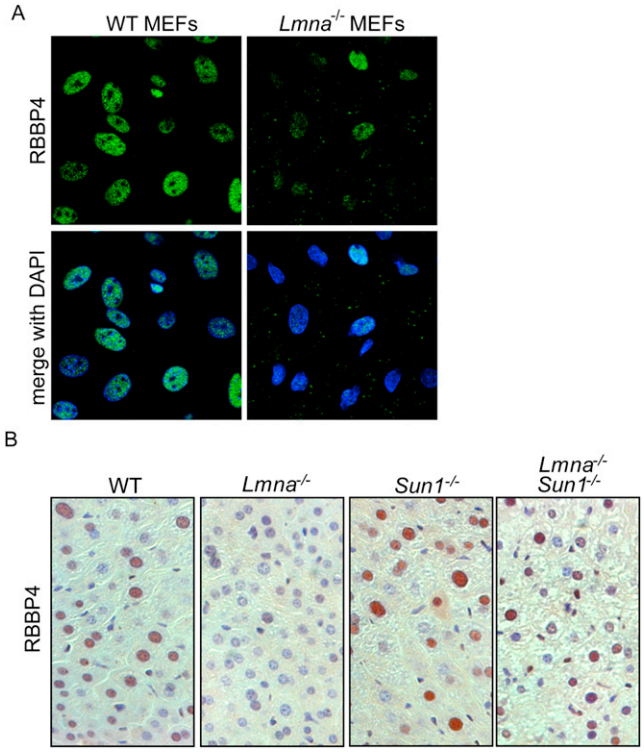

Figure S6. *Lmna*$^{-/-}$*Sun1*$^{-/-}$ and WT Mouse Liver Tissue Show More RBBP4 Staining Than *Lmna*$^{-/-}$ Liver Tissue, Related to Figure 7

(A) WT and *Lmna*$^{-/-}$ MEFs were stained with rabbit anti-RBBP4 (green). Note the reduced staining for RBBP4 in *Lmna*$^{-/-}$ MEFs. DAPI staining of DNA is in blue. (B) Liver tissue from WT, *Lmna*$^{-/-}$, *Sun1*$^{-/-}$ and *Lmna*$^{-/-}$*Sun1*$^{-/-}$ was stained with RBBP4 by immunohistochemistry. Brown signals show nuclear RBBP4 staining; note fewer numbers of "brown" nuclei in *Lmna*$^{-/-}$ liver compared to WT, *Sun1*$^{-/-}$ and *Lmna*$^{-/-}$*Sun1*$^{-/-}$ liver. Images are at 400 × magnification.